Analysis and Optimization of UAV Turning Methodology

Shengan Yang

Supervised by:
Prof. Meyer Nahon

Department of Mechanical Engineering
McGill University, Montréal

April 2022

A thesis submitted to McGill University in partial fulfillment of the requirements of the Undergraduate Honours Program

Abstract

The turning performance of unmanned aerial vehicles (UAVs) is analyzed with the aim of finding the most efficient turning method besides a coordinated turn. Based on the simulation, the performance of the coordinated turn and the zero roll turn are compared. The results indicate that the coordinated turn performs better in tighter turns (smaller radius with higher velocity) while the zero roll turn performs better in looser turns (larger radius with lower velocity). This is then followed by a systematic optimization-based study of steady and transient turns. Several scenarios are tested, leading to the conclusion that the coordinated turn performs the best in steady turns. In the case of transient turns, the turning methodology with sideslip is better than the coordinated turn. However, the coordinated turn still performs well if the requirements of turning are not too strict. In summary, the coordinated turn can be verified to be suitable for most turns.

Abrégé

Les performances de virage des véhicules aériens sans pilote (UAV) sont analysées dans le but de trouver la méthodologie de virage la plus efficace à part du virage coordonné. Utilisant une simulation, le virage coordonné et le virage sans roulis sont comparés. Ceci démontre que le virage coordonné fonctionne mieux dans les virages plus serrés tandis que le virage sans roulis fonctionne mieux dans les virages moins serrés. Puis, en utilisant un logiciel d'optimisation, plusieurs scénarios sont testés. Les résultats démontrent que le virage coordonné donne les meilleurs résultats dans les virages continus. Par contre, pour les virages transitoires, la méthodologie de virage avec dérapage est meilleure que le virage coordonné. Cependant, le virage coordonné fonctionne toujours bien si les exigences de virage ne sont pas trop strictes. Par conséquent, le virage coordonné convient à la plupart des virages.

Acknowledgements

First and foremost, I would like to express my sincere gratitude to my thesis supervisor, Professor Meyer Nahon, for his guidance over this research. He has given me great instruction and encouragement throughout this journey. The thesis could not have been finished without him.

Second, I would like to express my gratitude to the members of McGill Aerospace Mechatronics Lab, especially Jackson Empey, Juan Carlos Hernández Ramírez, Zihao Zhuo, Eitan Bulka, Joshua Levin, and Waqas Khan. I'm grateful to Jackson for spending extra time discussing my results with me almost every week. I thank Juan, Zihao, and Eitan for their advice when I got lost in my research. Though I never met Joshua and Waqas, I'm grateful for using the optimization setup and simulation model originally designed by them.

Third, I would like to extend my gratitude to my friends, especially Junrui Huang, Yilan Lu, Xiaoya Zhang, Lijing Wang, and Huiyi Wang who helped me through these eight months.

Fourth, my thanks also goes to the professors, such as Professor Evgeny Timofeev, who taught me, as well as the authors whose books and papers enlightened me during my research.

Finally, I would like to extend my gratitude to my family for their support of my studies. Their support encouraged me to continue when I met difficulties.

Contents

List of Figures

List of Tables

Chapter 1

Introduction

Unmanned aerial vehicles (UAVs) are aircraft without a human operator onboard. They can be controlled by a human operator remotely or autonomously [1]. Most UAVs are classified into four categories: rotor crafts, fixed-wing, flapping-wing, and hybrid UAVs [2]. In this thesis, the focus is on fixed-wing aircraft.

1.1 Background and Motivation

In essentially all flight mechanics studies of fixed-wing aircraft, the 'coordinated turn' is used as the basis for performing turns. These are turns in which the ailerons and the rudder are actuated synchronously, making the aircraft bank to some roll angle, to maintain zero lateral force in the aircraft frame, and zero sideslip [3]. The main reason for doing this in manned aircraft is that this results in the most comfortable type of turn for passengers, as well as minimizing the risk of entering a spin. However, UAVs have no occupants, so there is no need to be concerned with passenger comfort. Based on past flight testing of UAVs, pilots did not always use 'coordinated turn'. This may be due to the difficulty or inconvenience of actuating both ailerons and rudder synchronously in the remote control plane, or this may indicate that there exists another way to turn efficiently. The present research was motivated

by the following questions: What is the most efficient type of turn for fixed-wing UAVs? Is it necessary or beneficial to make the aircraft bank to turn?

1.2 Research Objectives

The primary objective of this thesis is to evaluate how an aircraft turns. We are interested in finding the most efficient way of turning for the aircraft in terms of precision and turn rate. The research is split into two parts: simulation and optimization. The simulation tool used extensively in this thesis was developed by Khan [4], and is discussed in Section 2.1. The simulation is used to gain insight into different turning methods. Following this, the simulation model is coupled to an optimization tool to run many cases to evaluate the turns in an attempt to find out whether there is an optimal way of turning. The result is compared with the theoretical analysis to evaluate whether the turning methodology is improved.

1.3 Literature Review

Some prior studies have considered the turning maneuver as a part of the motion planning process, such as [5]. By contrast, in the present work, the turning methodology is separate from motion planning and analyzed via optimization.

In [6], the authors optimized the trajectory for air races with high accuracy. In [7], two agile turn strategies, minimum travel distance turn and minimum radius turn, were evaluated through computer simulation. The shortest turning path was optimized in [8].

The banked turn in trim primitives shown in [9] is similar to the trim maneuver discussed in this thesis with different cost functions. The aggressive turn around in [9] is similar to a case shown in Section 5.1.

1.4 Thesis Structure

Chapter 1 introduces the background, motivation, objectives, and literature review of this research. In Chapter 2, the preliminary works needed in later chapters are introduced. A simulation is presented to analyze and compare the performance between a coordinated turn and a zero roll turn in Chapter 3. Chapters 4 and 5 investigate the trim and agile maneuver of turning via optimization, respectively. A conclusion and recommendations for future work are discussed in Chapter 6. All supplementary information is listed in Appendix. A.

Chapter 2

Preliminaries

This chapter discusses preliminary work used to support this thesis. The first section of this chapter briefly introduces the simulation model that was originally designed by Khan [4]. The simulation model is used as a tool towards achieving the objectives of this thesis. The detailed modeling process can be found in [4]. The second section of this chapter describes the optimization framework used in Chapters 4 and 5. The optimization setup is based primarily on the work done by Levin [9] with some modifications. The detailed optimization process he conducted previously can be found in [9].

2.1 Aircraft Model

2.1.1 Aircraft Configuration

As shown in Fig. 2.1, the UAV that this thesis analyzes is the McFoamy produced by West Michigan Park Flyers, which has a wingspan of 0.86 m and a mass of 0.45 kg. A more detailed listing of its properties is given in Appendix A.1. These will be used in the Section 2.1.3: equations of motion.

2.1.2 Reference Frames

Two frames used to describe an aircraft are the body frame and the inertial frame. The body frame is fixed to the aircraft while the inertial frame is fixed to the ground. They are both shown in Fig. 2.1.

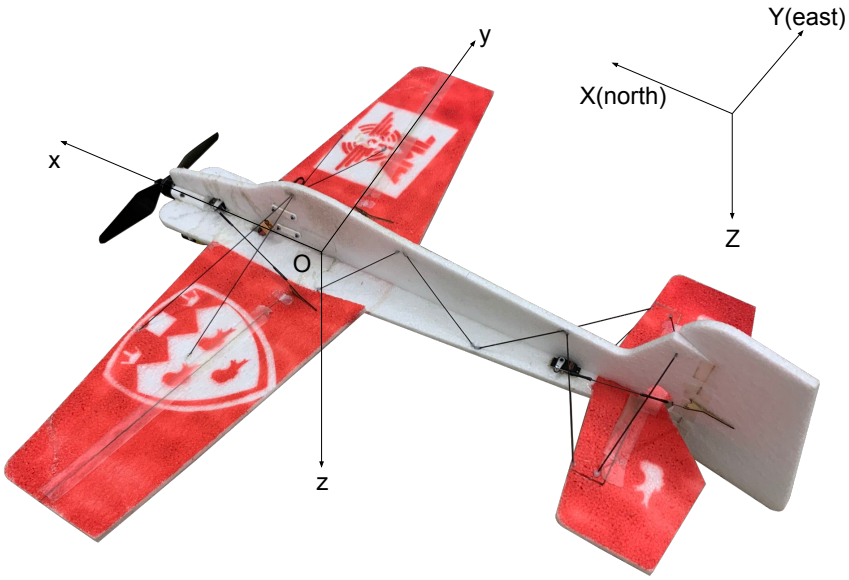

Figure 2.1: Inertial Frame (X, Y, Z) and Body Frame (x, y, z)

The body frame axes are labelled as Ox, Oy, and Oz, where O is the center of mass. The Ox axis points roughly in the forward direction, and Oy at a right angle to the plane of symmetry and towards the starboard wing tip. The Oz axis points roughly downwards [10]. The inertial frame is defined by three unit vectors, which are pointing north (X), east (Y), and downward (Z). The mass center position of the aircraft is denoted by $[x,\ y,\ z]^T$ in the inertial frame while its attitude is represented by Euler angles $[\phi,\ \theta,\ \psi]$, known as the roll, pitch and yaw angles. These angles are obtained by rotating the inertial frame to the body frame at the sequence of yaw (ψ) about Oz axis, pitch (θ) about Oy axis, and roll (ϕ) about Ox axis where rotation takes place about the axes from the previous rotation. The detailed

definition of the orientation can be found in [10]. Since there are two different frames, the rotation matrix $\mathbf{L}_{BI}$ is used to transform a vector from the inertial frame to the body frame.

$$\mathbf{L}_{BI} = \begin{bmatrix} \cos\psi\cos\theta & \sin\psi\cos\theta & -\sin\theta \\ \cos\psi\sin\theta\sin\phi - \sin\psi\cos\phi & \cos\psi\sin\theta\sin\phi + \cos\psi\cos\phi & \cos\theta\sin\phi \\ \sin\psi\sin\phi + \cos\psi\sin\theta\sin\phi & \cos\psi\sin\theta\cos\phi - \cos\psi\cos\phi & \cos\theta\cos\phi \end{bmatrix} \tag{2.1}$$

2.1.3 Equations of Motion

The equations of motion are the basis of the simulation and optimization. The aircraft is considered to be a rigid body; thus, the dynamics and kinematics equations are summarized as:

$$\mathbf{F}_B = m\left[\frac{\delta \mathbf{V}_B}{\delta t} + \boldsymbol{\omega}_B \times \mathbf{V}_B\right] \tag{2.2}$$

$$\mathbf{M}_B = \mathbf{I}\dot{\boldsymbol{\omega}}_B + \boldsymbol{\omega}_B \times \mathbf{I}_B\boldsymbol{\omega}_B \tag{2.3}$$

$$\dot{\mathbf{P}}_I = \mathbf{L}_{BI}^T \mathbf{V}_B \tag{2.4}$$

$$\begin{aligned} \dot{\phi} &= p + q\sin\phi\tan\theta + r\cos\phi\tan\theta \\ \dot{\theta} &= q\cos\phi - r\sin\phi \\ \dot{\psi} &= q\sin\phi\sec\theta + r\cos\phi\sec\theta \end{aligned} \tag{2.5}$$

where $V_B = [u,\ v,\ w]^T$ and $\omega_B = [p,\ q,\ r]^T$ are the translation and angular velocity, respectively. $F_B = [X,\ Y,\ Z]^T$ and $M_B = [L,\ M,\ N]^T$ are the net external forces and moments acting on the aircraft, respectively. $P_I = [x,\ y,\ z]$ is the position vector, and I_B is the moment of inertia matrix shown below. The last three equations relate the rate of change of the Euler angles to the angular velocity. The subscript $\boldsymbol{B}$ denotes the elements in the body

frame while the subscript $\boldsymbol{I}$ denotes elements in the inertial frame.

$$I_B = \begin{bmatrix} I_{xx} & -I_{xy} & -I_{xz} \\ -I_{xy} & I_{yy} & -I_{yz} \\ -I_{xz} & -I_{yz} & I_{zz} \end{bmatrix} \tag{2.6}$$

The detailed expansion of the equations of motion using Euler angles, Eq. 2.2, 2.3, and 2.4 are shown below:

$$\begin{aligned}
\dot{u} &= \frac{F_x}{m} - g\sin\theta + rv - qw \\
\dot{v} &= \frac{F_y}{m} + g\sin\phi\cos\theta + pw - ru \\
\dot{w} &= \frac{F_z}{m} + g\cos\phi\cos\theta + qu - pv \\
\dot{p} &= \frac{I_{zz}M_x + I_{xz}M_z - I_{xz}\left(I_{yy} - I_{xx} - I_{zz}\right)pq - \left(I_{xz}^2 + I_{zz}\left(I_{zz} - I_{yy}\right)\right)qr}{I_{xx}I_{zz} - I_{xz}^2} \\
\dot{q} &= \frac{M_y - \left(I_{xx} - I_{zz}\right)pr - I_{xz}\left(p^2 - r^2\right)}{I_{yy}} \\
\dot{r} &= \frac{I_{xz}M_x + I_{xx}M_z - I_{xz}\left(I_{yy} - I_{xx} - I_{zz}\right)qr - \left(I_{xz}^2 + I_{xx}\left(I_{xx} - I_{yy}\right)\right)pq}{I_{xx}I_{zz} - I_{xz}^2} \\
\dot{\phi} &= p + q\sin\phi\tan\theta + r\cos\phi\tan\theta \\
\dot{\theta} &= q\cos\phi - r\sin\phi \\
\dot{\psi} &= q\sin\phi\sec\theta + r\cos\phi\sec\theta \\
\dot{x} &= u\cos\psi\cos\theta + v\left(\cos\psi\sin\theta\sin\phi - \sin\psi\cos\phi\right) + w\left(\sin\psi\sin\phi + \cos\psi\sin\theta\cos\phi\right) \\
\dot{y} &= u\sin\psi\cos\theta + v\left(\sin\psi\sin\theta\sin\phi + \cos\psi\cos\phi\right) + w\left(-\cos\psi\sin\phi + \sin\psi\sin\theta\cos\phi\right) \\
\dot{z} &= -u\sin\theta + v\cos\theta\sin\phi + w\cos\theta\cos\phi
\end{aligned} \tag{2.7}$$

In addition, the entire simulation model also consists of the thruster model, propeller slipstream model, aerodynamics model, and the feedback controller. For the sake of brevity, we do not introduce them here. Interested readers can consult [4] for more information.

2.2 Optimization Setup

From a broader perspective, this section describes the joint optimization setup that will be utilized in Chapters 4 and 5. Specifically, Chapter 4 evaluates the trim maneuver, which is a steady flight with constant control inputs. On the other hand, Chapter 5 analyses the agile maneuver in which control input changes with time.

The optimization problems discussed in this thesis belong to the optimal control problem, which has the following general framework [11]:

The cost function is:

$$J = g\left[\mathbf{x}\left(t_0\right), t_0, \mathbf{x}\left(t_f\right), t_f\right] + \int_{t_0}^{t_f} f[\mathbf{x}(t), \mathbf{u}(t), t]\mathrm{d}t \tag{2.8}$$

subject to the dynamic constraints

$$\dot{\mathbf{x}}(t) = \mathbf{a}[\mathbf{x}(t), \mathbf{u}(t), t], \tag{2.9}$$

the path constraints

$$\mathbf{h}[\mathbf{x}(t), \mathbf{u}(t), t] \leq \mathbf{0} \tag{2.10}$$

and the endpoint conditions

$$\mathbf{e}\left[\mathbf{x}\left(t_0\right), t_0, \mathbf{x}\left(t_f\right), t_f\right] = 0 \tag{2.11}$$

where $\mathbf{x}(t)$ and $\mathbf{u}(t)$ are the state vector and control vector. The symbols g, f, a, h, and e all represent functions.

Following the previous work done by Levin [9], the state vector of the aircraft is set as:

$$\mathbf{x} = [u,\ v,\ w,\ p,\ q,\ r,\ \phi,\ \theta,\ \psi,\ x,\ y,\ z,\ \delta_a,\ \delta_e,\ \delta_r,\ T]^T \tag{2.12}$$

where $\delta_a,\ \delta_e,\ \delta_r,\ T$ represents the control inputs of ailerons, elevator, rudder, and thrust, respectively. The first three control inputs are the angles of the surface deflections, which are measured in degrees. The thrust is represented by the rotation speed of the motor, which is measured in revolution per minute (rpm). Other terms are the same as introduced before. It should be noted that the Euler angles are measured in radian.

The control vector consists of the derivatives of the four control inputs because it allows extra constraints for the changing rate of the control inputs, which is especially necessary in Chapter 4

$$\mathbf{u} = [\dot{\delta}_a,\ \dot{\delta}_e,\ \dot{\delta}_r,\ \dot{T}]^T \tag{2.13}$$

2.2.1 Dynamic Constraints

As shown in Eq. 2.9, the dynamic constraints connect the state vector and the control vector to the derivative of the state vector. Since there are 16 elements in the state vector, there are 16 derivative equations related to them. The first 12 derivative equations are equations of motion, 2.7, shown in Section 2.1.3. Meanwhile, the derivatives of the last four control inputs in the state vector are related to the control vector as shown below:

$$\begin{aligned} \dot{\delta}_a &= u_{\delta_a} \\ \dot{\delta}_e &= u_{\delta_e} \\ \dot{\delta}_r &= u_{\delta_r} \\ \dot{T} &= u_T \end{aligned} \tag{2.14}$$

It should be noted that forces and moments are needed in the equations of motion. They are generated by the aircraft model described in Section 2.1. Additionally, the controller of the aircraft model is removed because we want the optimization to be fully in charge of determining the control inputs. The forces and moments generated in the body frame at different states are generated as follows:

$$[F_x,\ F_y,\ F_z,\ M_x,\ M_y,\ M_z] = M\,[\delta_a,\ \delta_e,\ \delta_r,\ T,\ u,\ v,\ w,\ p,\ q,\ r] \tag{2.15}$$

where M represents the aircraft model.

The dynamic constraints are directly applied in Chapter 4. In Chapter 5, the Euler angles are replaced by quaternions due to the potential for singularities when using Euler angles at extreme attitudes. The detailed setup will be clarified again in Chapters 4 and 5.

2.2.2 Path Constraints

Path constraints are those applied to the entire process. The common path constraints in Chapters 4 and 5 are from the geometry and performance of the McFoamy. The deflection angles of ailerons, elevator, and rudder are limited due to the structure of the aircraft. Meanwhile, since servo motors are used to actuate the control surfaces, the rates of actuating them are limited by the limitations of the servo motors. Furthermore, both motor and battery limit the rotational speed and acceleration of the propeller. The path constraints are expanded as:

$$\begin{aligned}
-\delta_{a_{max}} \leq & \delta_a \leq \delta_{a_{max}} \\
-\delta_{e_{max}} \leq & \delta_e \leq \delta_{e_{max}} \\
-\delta_{r_{max}} \leq & \delta_r \leq \delta_{r_{max}} \\
T_{min} \leq & T \leq T_{max} \\
-\dot{\delta}_{a_{max}} \leq & \dot{\delta}_a \leq \dot{\delta}_{a_{max}} \\
-\dot{\delta}_{a_{max}} \leq & \dot{\delta}_a \leq \dot{\delta}_{a_{max}} \\
-\dot{\delta}_{a_{max}} \leq & \dot{\delta}_a \leq \dot{\delta}_{a_{max}} \\
-\dot{T}_{max} \leq & \dot{T} \leq \dot{T}_{max}
\end{aligned} \tag{2.16}$$

The detailed values of the parameters are shown in Appendix. A.1.

2.2.3 Optimization Solver

As shown previously in Section 2.1, the aircraft model involves many nonlinear equations, which makes the whole system extremely nonlinear; thus, it is impossible to solve the optimization analytically. The only feasible way to solve such optimal control problem is through numerical methods. In this thesis, a general-purpose MATLAB software for solving optimal control problems, GPOPS-II [12], is selected as the solver. It transforms the optimal control problem to a nonlinear programming problem (NLP). Furthermore, GPOPS-II calls the NLP solver, SNOPT [13], to solve the optimization problems automatically.

2.3 Coordinated Turn

The turning of the aircraft is similar to circular motion in a plane, which requires the generation of a centripetal force. In the coordinated turn, centripetal force is generated purely from the lift. As shown in Fig. 2.2, the aircraft performing the coordinated turn will bank to a roll angle specified in Eq. 2.17. This results in the lift having a component directed towards the center of the turning. Meanwhile, in the vertical direction, the component of the lift is equal to the weight of the aircraft. In this thesis, the lift is always perpendicular to the aircraft's velocity and points upward.

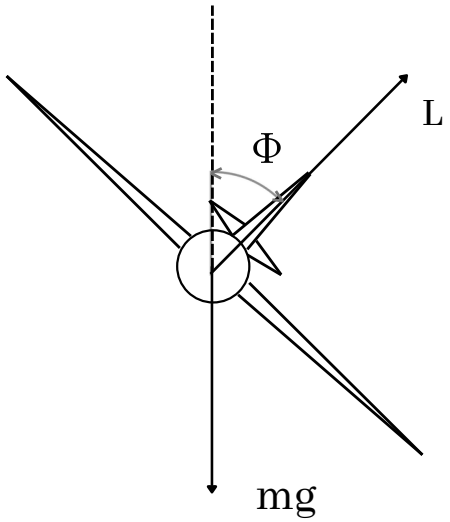

Figure 2.2: Coordinated Turn

The roll angle in the coordinated turn is defined as:

$$\phi = \tan^{-1}(\frac{V^2}{rg}) \tag{2.17}$$

where ϕ is the roll angle, V is the aircraft velocity, r is the radius, and g is the gravitational acceleration.

By contrast, in a zero roll turn, the turn is performed without any bank; the roll angle is 0°.

Another feature of the coordinated turn is that it has zero sideslip, which is the velocity in the y direction of the body frame. The sideslip angle is defined as:

$$\beta = \sin^{-1}(\frac{v_B}{V}) \tag{2.18}$$

where v_B is the velocity in the y direction of the body frame, and V is the aircraft total velocity.

Chapter 3

Simulation

In this chapter, the simulation is used to test the ability of the aircraft turning in different circumstances. It is operated manually to compare two different types of turns: coordinated turn and zero roll turn.

3.1 Path Setup

The simulation is configured to prescribe a tracking point and make the aircraft follow it using an existing controller [4]. As the users of the simulation, we only set how the tracking point moves. The controller manages how the control surfaces should be actuated to follow the tracking point automatically and adjusts the aircraft's attitude to make sure that the aircraft follows the tracking point closely. For this research, the tracking point is set to go straight for some time and then make a circular turn with a specific radius, all while maintaining a constant velocity. As shown in Fig. 3.1, the velocity is set to be 7 m/s. The radius is set to be 10 m. The blue dash line shows the path of the tracking point, hereafter called the 'reference path'. The red line shows the path of the aircraft when using the default controller described in [14]. This controller prescribes a roll angle that aims to reduce the aircraft's cross-track error.

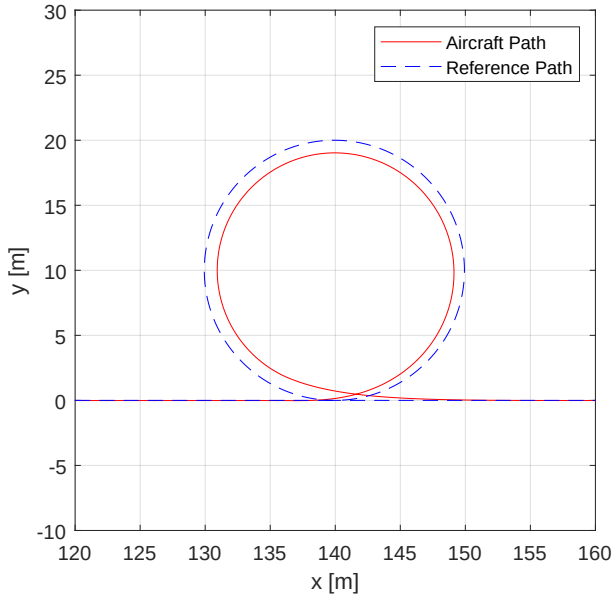

Figure 3.1: Aircraft Turn ($V = 7\ m/s$, $r = 10\ m$)

3.2 Path Error

As shown in Fig. 3.1, a difference can be observed between the aircraft path and the reference path, which is understandable because the aircraft cannot follow the tracking point exactly due to the lag and limited aircraft performance. The difference is more obvious in extreme cases, which will be shown later. It is reasonable to assess the turning performance by determining how close the aircraft follows the tracking point. Therefore, the path error is defined as the average of the distance from a point in the aircraft path to the closest point in the reference path. In this thesis, we only consider the turn, so the path error is calculated starting from the time that the aircraft turns, and ends when the aircraft's yaw angle is within a half degree of the yaw angle before the turn started. The yaw angle is used here to determine whether the aircraft points in almost the same direction before it enters the turn. Once the yaw angle is almost the same, we consider the aircraft to have completed a 360° turn.

For a point i on the aircraft path, the instantaneous distance error from the reference path is calculated as:

$$e_i = \sqrt{(x_i - x_r)^2 + (y_i - y_r)^2 + (z_i - z_r)^2} \tag{3.1}$$

where $[x_i,\ y_i,\ z_i]^T$ is the position of the point i, $[x_r,\ y_r,\ z_r]^T$ is the position of the point on the reference path that is closest to the point i. The path error is then calculated as the root mean square of the instantaneous error:

$$E = \sqrt{\frac{\sum_{i=1}^{n} {e_i}^2}{n}} \tag{3.2}$$

where n is the number of points in the turn.

3.3 Result Comparison

We are interested to find out whether there is an alternative to the coordinated turn that can perform the turn more efficiently. As mentioned in Section 2.3, these two turning methods have their unique roll angles. In this case, the roll angle is specified by the user as a setpoint to the controller to replace the roll angle setpoint of the default controller described in Section 3.1. After setting velocity, radius, and the roll angle, the simulation provides insight into how the aircraft reacts towards different turns.

Fig. 3.2 and 3.3 are some examples of the aircraft and reference paths for moderate turn conditions at a speed of 7 m/s and a turn radius of 15 m. In these conditions, both the coordinated and zero roll turns perform well. The path error of the zero roll turn is slightly better.

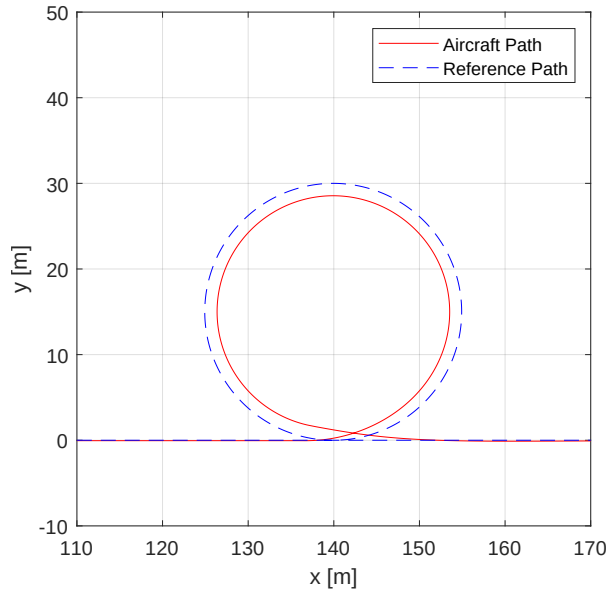

Figure 3.2: Coordinated Turn ($V = 7\ m/s$, $r = 15\ m$)

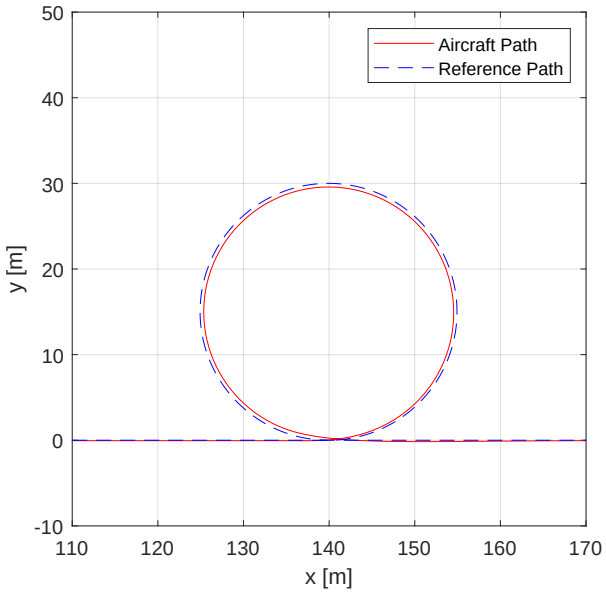

Figure 3.3: Zero Roll Turn ($V = 7\ m/s$, $r = 15\ m$)

The following two cases show less successful turns. When the velocity is set to 7 m/s, the radius is set to 5 m, the aircraft no longer follows the tracking point well. The path error is significant. The coordinated turn performs better in these conditions.

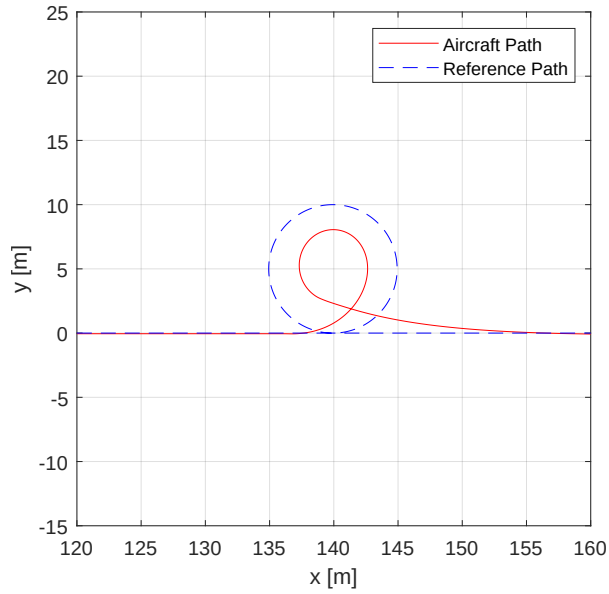

Figure 3.4: Coordinated Turn ($V = 7\ m/s$, $r = 5\ m$)

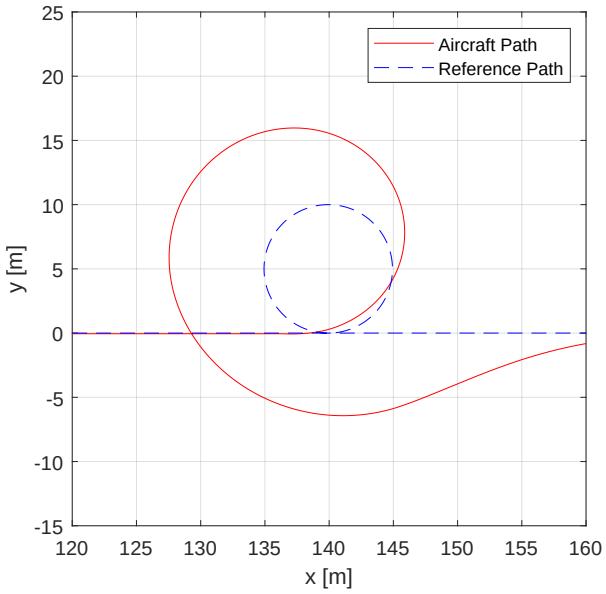

Figure 3.5: Zero Roll Turn ($V = 7\ m/s$, $r = 5\ m$)

Table 3.1 shows the rms path error at different velocities and turning radii. The first column in each velocity is the result of the coordinated turn. The second column in each velocity is the result of the zero roll turn.

Velocity / Radius	7		9		11		13		15	
5	1.2706	3.2408	1.3485	4.5508	1.685	6.8655	2.3035	9.7766	3.1156	12.7089
10	1.3491	0.58317	1.563	1.0195	1.6429	0.56705	1.9118	1.1191	2.2879	2.3163
15	1.0569	0.29132	1.4286	0.68838	1.8723	1.2052	2.1142	1.7903	2.5091	2.3759
20	0.85167	0.14975	1.2439	0.44315	1.7558	0.90635	2.3140	1.4893	2.6776	2.1496
25	0.70426	0.07351	1.0752	0.29381	1.5976	0.68838	2.2307	1.2334	2.8428	1.8922

Table 3.1: RMS Path Error

To get a more intuitive view of the results in Table 3.1, they are plotted in Figures 3.6 and 3.7 below.

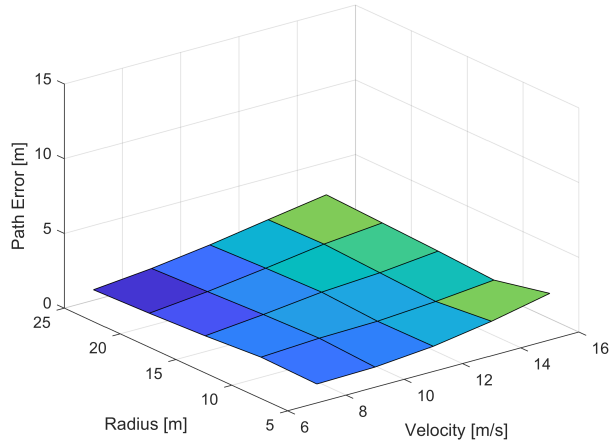

Figure 3.6: RMS Error for Coordinated Turns

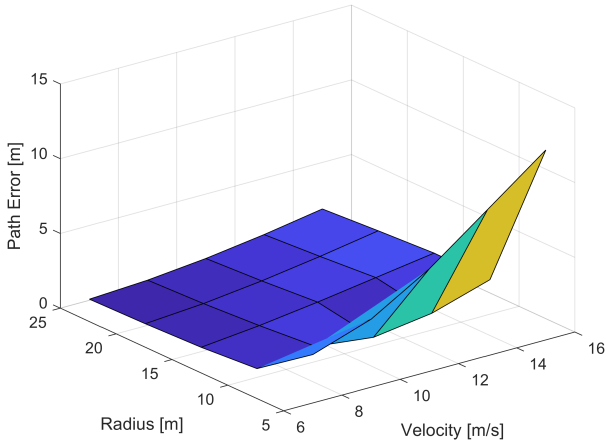

Figure 3.7: RMS Error for Zero Roll Turns

It can be observed that the coordinated turn performs better for turns with a smaller radius and higher velocity. Conversely, the zero roll turn performs better for larger radius turns at slower velocity. It verifies that there may be some turning methods perform better than the coordinated turn in some scenarios. To further investigate turning strategies, the following chapters will make use of an optimization-based approach.

Chapter 4

Optimization of Trim Maneuver

The trim maneuver of turning at the constant height (henceforth 'trim maneuver') is a steady maneuver, in which the control inputs remain constant during the whole process. Since the control inputs do not change, the trim maneuver is easier to understand and so is studied first.

In this chapter, the turning trim maneuver is analyzed using optimization. Discussed generally in Section 2.2, the optimization problem is further defined here. The state vector and the control vector remain the same as Eq. 2.12 and 2.13. The cost function, Eq. 2.8, is specified in each section later. The dynamics constraints, Eq. 2.9, remain the same as the equations of motion. The path constraints, Eq. 2.10, become:

$$\begin{aligned} V &= u^2 + v^2 + w^2 = V_d \\ \mathbf{u} &= [\dot{\delta}_a,\ \dot{\delta}_e,\ \dot{\delta}_r,\ \dot{T}]^T = \mathbf{0} \end{aligned} \tag{4.1}$$

where $[u,\ v,\ w]$ is the velocity in the body frame, V_d is the desired velocity set by the user. For this chapter, V_d is always set to be 10 m/s. $[\dot{\delta}_a,\ \dot{\delta}_e,\ \dot{\delta}_r,\ \dot{T}]^T$ is the derivatives of the control inputs, which remains at zero so the control inputs do not change.

The endpoint constraint, Eq. 2.11, becomes:

$$\begin{aligned} \mathbf{x}(t_0) &= [u,\ v,\ w,\ p,\ q,\ r,\ \phi,\ \theta,\ 0,\ 0,\ 0,\ 0,\ \delta_a,\ \delta_e,\ \delta_r,\ T]^T \\ \mathbf{x}(t_f) &= [u,\ v,\ w,\ p,\ q,\ r,\ \phi,\ \theta,\ 2\pi,\ x,\ y,\ z,\ \delta_a,\ \delta_e,\ \delta_r,\ T]^T \\ t_f &= t_d \end{aligned} \tag{4.2}$$

For the initial condition, the yaw angle is set to be zero, and the initial position is set to be the origin. For the final condition, only the yaw angle is set to be 2π, which indicates that the aircraft turns 360°. The final time is t_d set by the user. In this case, the turning rate or yaw rate in °/s is simply defined by the final time as:

$$\dot{\psi} = \frac{360}{t_f} \tag{4.3}$$

In this way, the yaw rate is defined by the user. In this chapter, we consider yaw rates from 10 °/s to 110 °/s in steps of 10 °/s.

Fig. 4.1 shows the trajectory of the aircraft when the yaw rate is set to be 100 °/s ($t_f = 3.6\ s$), the velocity is set to be 10 m/s. The cost function is given by Eq. 4.6.

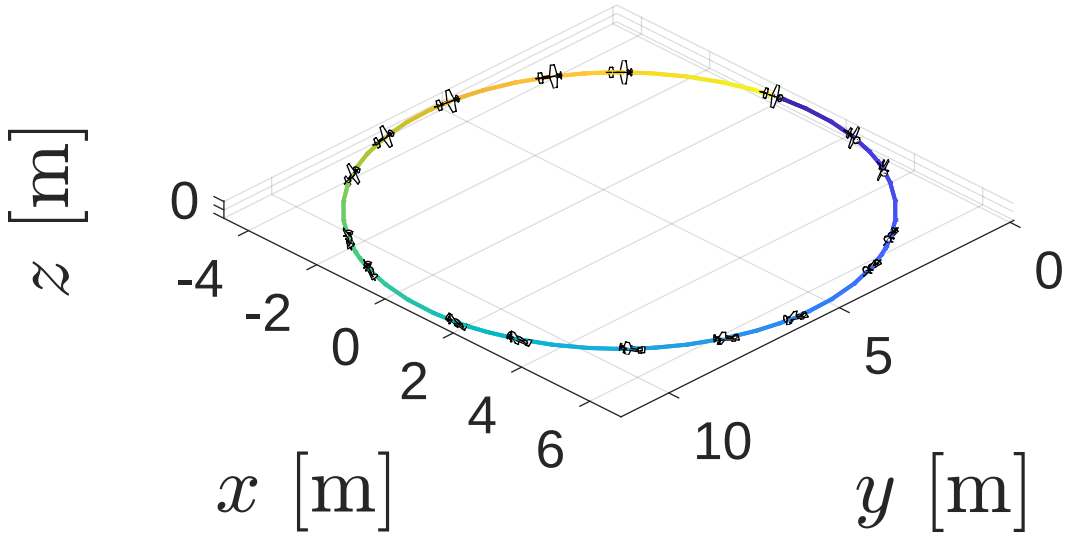

Figure 4.1: Aircraft Turn ($V = 10\ m/s$, $\dot{\psi} = 100\ °/s$, minimize thrust)

The trim turning maneuver is considered to be a constant circular motion, which is also confirmed by the trajectory shown in Fig. 4.1. The turn radius is calculated as:

$$r = \frac{Vt_f}{2\pi} \tag{4.4}$$

At this turn radius, the corresponding roll angle of the coordinated turn, Eq. 2.17, becomes:

$$\phi = \tan^{-1}\left(\frac{2\pi V}{t_f g}\right) \tag{4.5}$$

4.1 Thrust Minimization

Thrust is the main consumption of energy, therefore rendering it a reasonable cost function. The cost function, Eq. 2.8, becomes:

$$J = T\left(t_f\right)^2 \tag{4.6}$$

Since the control inputs are constant, minimizing the thrust in the final state also minimizes thrust throughout turn. The yaw rate is set to vary from 10 °/s to 110 °/s in steps of 10 °/s. The velocity of the aircraft is set to be 10 m/s.

Fig. 4.2a shows the roll angle from the optimization as a function of yaw rate as a blue line. The roll angle calculated from the coordinated turn equation, Eq. 4.5, is shown in red dashed line. They are almost the same, which implies that the result from the optimization is the coordinated turn. Meanwhile, the sideslip angle plotted in Fig. 4.2b also verifies this assumption. The sideslip angle is negligible as it is smaller than one degree for all cases. The control inputs are shown in Fig. 4.2c and 4.2d. It can also be noticed that there is a sudden increase in all the plots except for the thrust around the yaw rate of 90 °/s. This is partially due to the step of the yaw rate chosen as 10 °/s. When the step of the yaw rate is changed to

1 °/s, it is found that the increase happens at the yaw rate of 88 °/s. The roll angle from the optimization is larger than the one calculated, but is still within one degree. The detailed plot can be found in Appendix A.3.

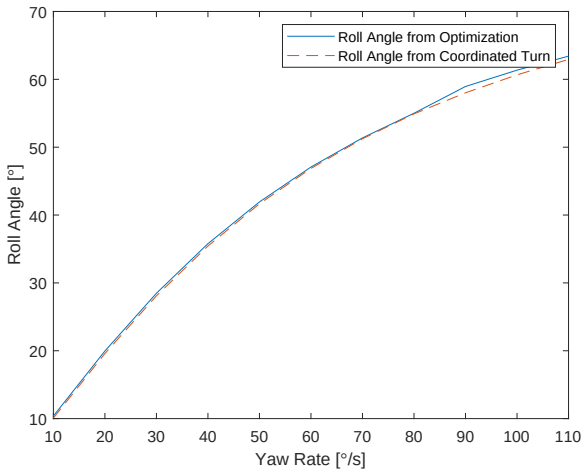

(a) Roll Angle vs. Yaw Rate

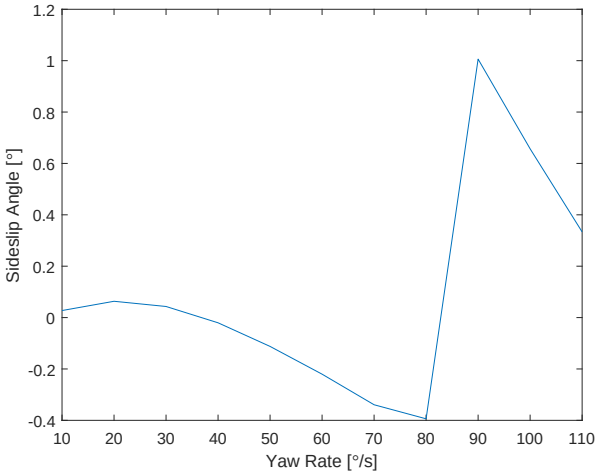

(b) Sideslip Angle vs. Yaw Rate

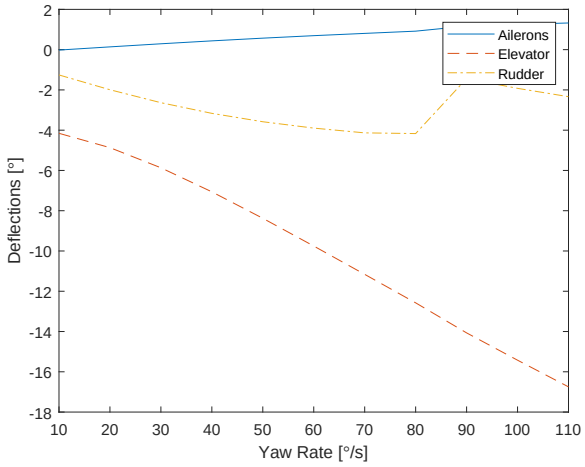

(c) Deflections vs. Yaw Rate

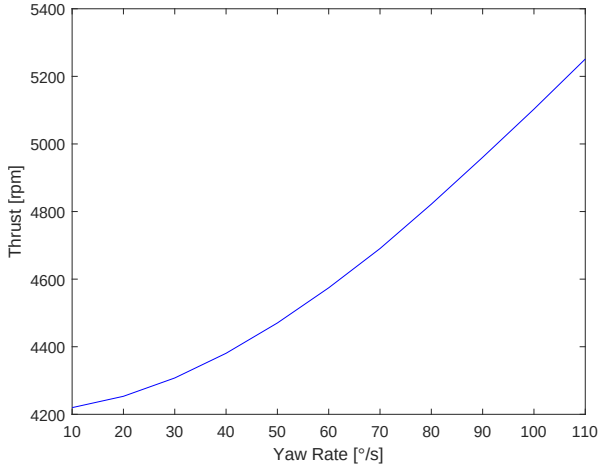

(d) Thrust vs. Yaw Rate

Figure 4.2: Results for Thrust Minimization

4.2 Deflections Minimization

It is possible that there is more than one way of actuating the control surfaces to achieve the same trim condition. We now consider the case in which the actuation is minimized. Similar to before, the yaw rate is set to vary from 10 °/s to 110 °/s at the step of 10 °/s. The velocity

of the aircraft is set to be 10 m/s. The cost function, Eq. 2.8, only involves the final state actuation:

$$J = \delta_a \left(t_f\right)^2 + \delta_e \left(t_f\right)^2 + \delta_r \left(t_f\right)^2 \tag{4.7}$$

As before, minimizing the deflections at the final time also minimizes them throughout the flight. Fig. 4.3a shows the roll angle (blue line) from the optimization and the roll angle from the coordinated turn equation (red dashed line). It can be observed that there is a gap between them. However, the difference between two lines is only a few degrees, which is still negligible. Meanwhile, the sideslip angle plotted in Fig. 4.3b is smaller than 1.8° for all cases, and the result is still close enough to the coordinated turn. The control inputs are shown in Fig. 4.3c and 4.3d. Compared to the control inputs in Section 4.1, the rudder is deflected less, which may cause the sideslip since the rudder and ailerons are not precisely coordinated.

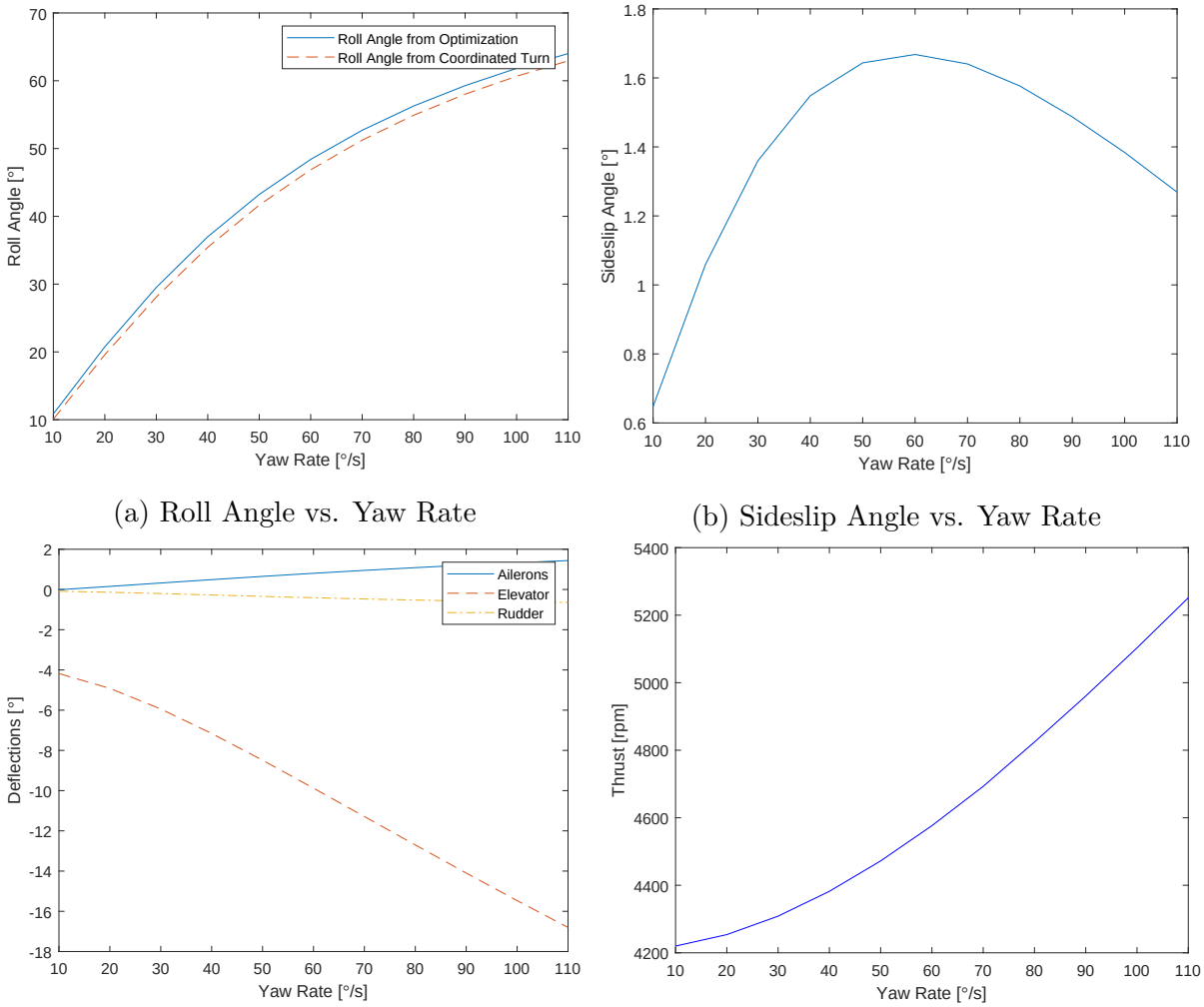

(a) Roll Angle vs. Yaw Rate

(b) Sideslip Angle vs. Yaw Rate

(c) Deflections vs. Yaw Rate

(d) Thrust vs. Yaw Rate

Figure 4.3: Results for Deflections Minimization

4.3 Turning Rate Maximization

It is also worth investigating the limit of the turning rate that the aircraft can achieve. The velocity of the aircraft is set to be 10 m/s. The cost function, Eq. 2.8, is set to be the final time:

$$J = t_f \tag{4.8}$$

The result of the optimization shows that the minimized final time is 1.3681 seconds, which indicates that the maximum turning rate is 263.1 °/s. Fig. 4.4a shows the roll angle (red

circle) from the optimization and the roll angle from the coordinated turn equation (blue asterisk). The difference between them is less than 0.1°. Meanwhile, the sideslip angle plotted in Fig. 4.4b is smaller than 1.5°. The result is still considered to be a coordinated turn. The control inputs are shown in Fig. 4.4c and 4.3d. Both the thrust and elevator reach the maximum, which are the cases of the limit of the aircraft turning performance in the trim maneuver.

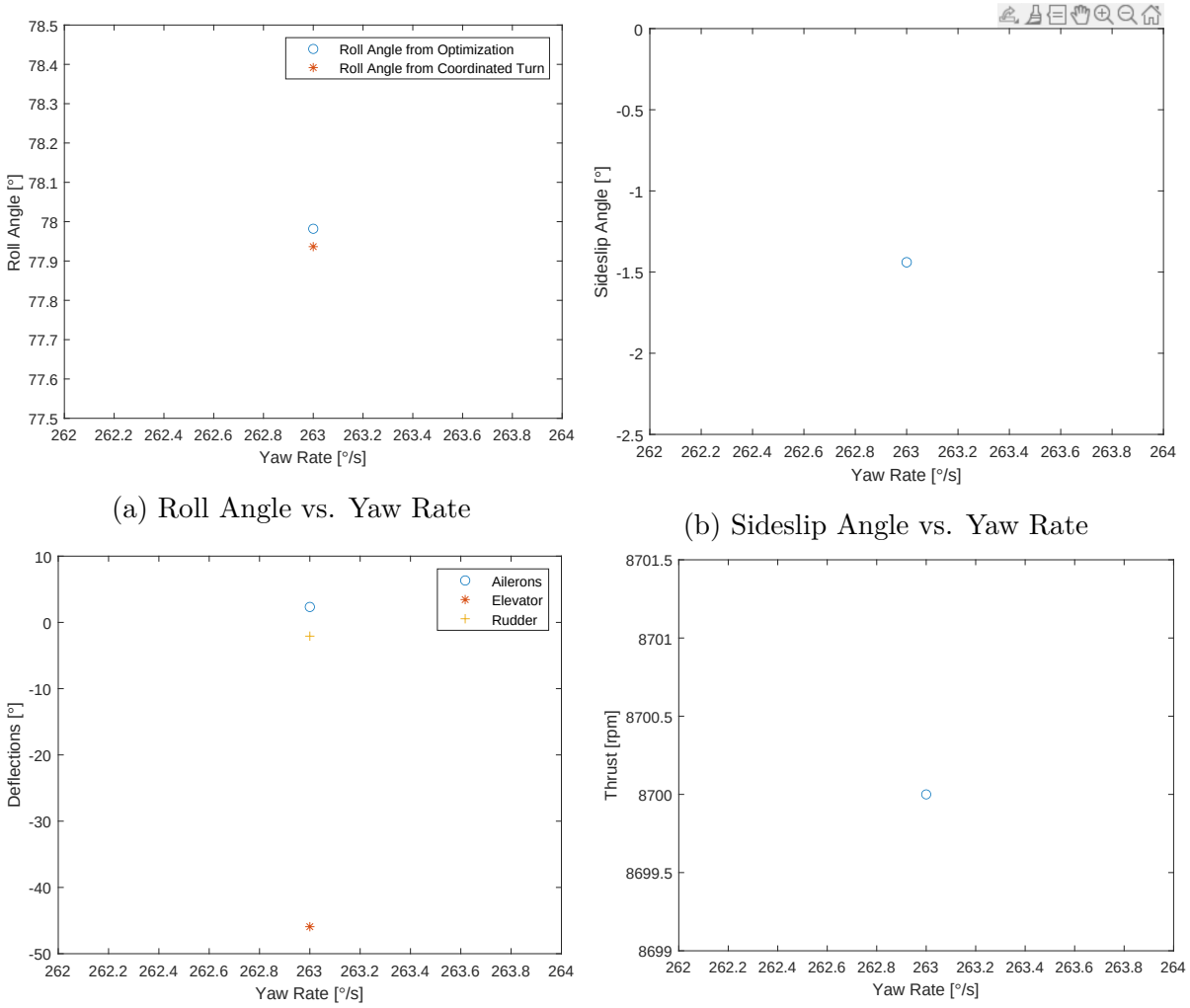

(a) Roll Angle vs. Yaw Rate

(b) Sideslip Angle vs. Yaw Rate

(c) Deflections vs. Yaw Rate

(d) Thrust vs. Yaw Rate

Figure 4.4: Results for Turning Rate Maximization

Some other cost functions are also tested, such as the minimax optimization of the control

surface deflections:

$$J = \max\left(|\delta_a|,\ |\delta_e|,\ |\delta_r|\right) \tag{4.9}$$

The results of all cost functions tend to be close to the coordinated turn, which leads to that the coordinated turn performs best in steady turns. Those results are not shown here for the sake of brevity.

Chapter 5

Optimization of Agile Maneuver

In this chapter, the optimization is used to determine how fast an aircraft can turn around without the previous constraints on the control inputs rates. Such transient turn maneuvers are henceforth called an agile maneuver. It is possible that the attitude during these maneuvers will be extreme, and so Euler angles are no longer used due to possible singularities. Instead, quaternions ($\boldsymbol{q} = [q_1,\ q_2,\ q_3,\ q_4]$) are used to represent the aircraft's orientation. The state vector becomes:

$$\mathbf{x} = [u,\ v,\ w,\ p,\ q,\ r,\ q_1,\ q_2,\ q_3,\ q_4,\ x,\ y,\ z,\ \delta_a,\ \delta_e,\ \delta_r,\ T]^T \tag{5.1}$$

The control vector does not change. The dynamics constraints still consist of the equations of motion and control derivative equations. The equations of motion are changed accordingly. The detailed expansion is shown in Appendix A.2. The control derivative equations remain the same as Eq. 2.14. The cost function, Eq. 2.8, is set to be the final time for all the cases in this chapter since only the turning performance is concerned:

$$J = t_f \tag{5.2}$$

The path constraint is from the feature of the quaternion:

$$q_1^2 + q_2^2 + q_3^2 + q_4^2 = 1 \tag{5.3}$$

The aircraft is set to fly northwards at the level height, then turn around (turn 180°) back to the straight level flight in the opposite direction (southwards). In this chapter, the initial state is defined as flying straight at level height with total velocity of 10 m/s. Such straight level flight is a kind of trim maneuver, which is established the same way as in Chapter 4. The detailed setup can be found in Appendix. A.4. The endpoint constraints, Eq. 2.11, become:

$$\begin{aligned} \mathbf{x}(t_0) &= [u_0,\ v_0,\ w_0,\ 0,\ 0,\ 0,\ q_{10},\ q_{20},\ q_{30},\ q_{40},\ 0,\ 0,\ 0,\ \delta_{a0},\ \delta_{e0},\ \delta_{r0},\ T_0]^T \\ \mathbf{x}(t_f) &= [u_0,\ v_0,\ w_0,\ 0,\ 0,\ 0,\ q_{1f},\ q_{2f},\ q_{3f},\ q_{4f},\ x_f,\ y_f,\ z_f,\ \delta_{a0},\ \delta_{e0},\ \delta_{r0},\ T_0]^T \end{aligned} \tag{5.4}$$

where subscript *0* indicates the term in the initial condition (straight level flight at 10 m/s), subscript *f* specifies that term in final state. $[q_1, q_2, q_3, q_4]$ represents the aircraft flying straight towards north with some pitch angle to maintain the level height. $[q_f, q_f, q_f, q_f]$ represents the aircraft flying the same condition but opposite direction. $[\delta_{a0},\ \delta_{e0},\ \delta_{r0},\ T_0]$ are the control inputs needed to maintain the aircraft flying at the initial condition. $[u_0,\ v_0,\ w_0]$ are the velocities in the body frame at the initial condition. The detailed values are shown in Appendix. A.4.

Quaternions are hard to analyze directly. For this reason, they are converted back to Euler angles when we investigate the maneuver. It can be noticed that there is more than one way of defining an attitude by Euler angles. For example, pitching 170° is the same as yawing 180°, pitching 10°, and rolling 180°. In this case, the pitch angle is manually limited to be less than 90° in the conversion process. Notably, the limit in the conversion process does not apply to the code used in the optimization, the aircraft still can pitch more than 90°.

5.1 Turning Back to the Origin

In this section, the final position is set to be the origin ($[x_f, y_f, z_f] = [0, 0, 0]$). The aircraft needs to turn around and return to the exact starting position. One possible scenario for this maneuver is that the aircraft approaches a dead end and needs to turn around rapidly.

5.1.1 Turn Without Constraints

In this section, no limits are set for the agile turn around back to the origin. The final time can be minimized to 1.4163 seconds. The maneuver trajectory, Euler angles, control inputs, and velocities for this maneuver are shown in Fig. 5.1a, 5.1b, 5.1c, and 5.1d, respectively. The axes in the trajectory plot are the inertial frame axes, positive x direction points north, positive y direction points east, and negative z direction points upward.

The trajectory shows that the aircraft performs a left turn around with height increase, then comes back. The aircraft tends to pitch up dramatically, accompanying roll and yaw during the turn. At around 0.5 seconds, the roll angle seen in Fig. 5.1b is depicted to experience a sudden increase from negative 143° to positive 180° due to the singularity of the angle. However, this does not mean that the aircraft suddenly rolled over; positive 180° and negative 180° both mean that the aircraft is experiencing the same attitude upside down. The same situation happens to the yaw angle. Both positive and negative 180° show that the aircraft points backward. The aircraft tends to be upside down to make the lift point downwards and decrease the height to back to the origin.

As shown in Fig. 5.1c, the rotational velocity of the propeller increases and reaches the maximum around the middle time. This is reasonable because the aircraft needs the maximum thrust force to make the fastest turn around. It can also be observed that when the thrust reaches the maximum, the aircraft heads backward roughly (shown as the yaw angle is around positive or negative 180°), and the total velocity is around the minimum. The maximum thrust points backward to oppose the original speed in the positive x direction to

make the aircraft turn back. The same situation happens in all cases below.

The sideslip angle in this scenario is very large as the aircraft tends to use sideslip to perform a fast turn around.

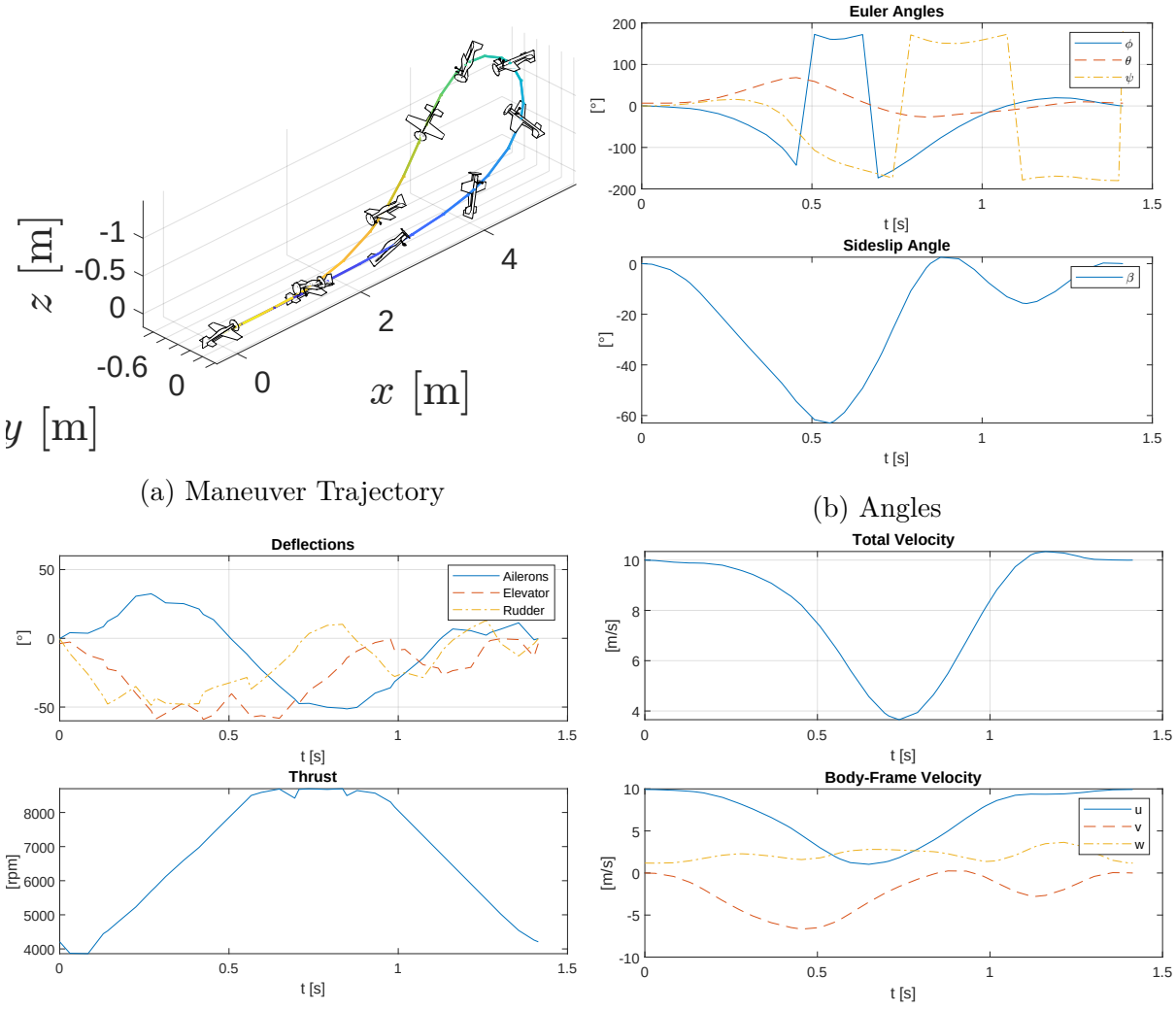

(a) Maneuver Trajectory

(b) Angles

(c) Control Inputs

(d) Velocities

Figure 5.1: Turning Back to the Origin Without Constraints

5.1.2 Turn With Euler Angles Constraints

Two of the Euler angles, pitch and roll angles, are constrained to be less than 90° to prevent the aircraft turning too aggressively. In this case, the final time can be minimized to 1.8261 seconds. The maneuver trajectory, Euler angles, control inputs, and velocities are shown in

Fig. 5.2a, 5.2b, 5.2c, and 5.2d, respectively. It can be observed that the same pattern between thrust, total velocity, and heading of the aircraft, which is explained before in Section 5.1.1. Once again, the sideslip is very large.

It can be observed that the aircraft still tends to roll as much as possible to generate the highest centripetal force from lift.

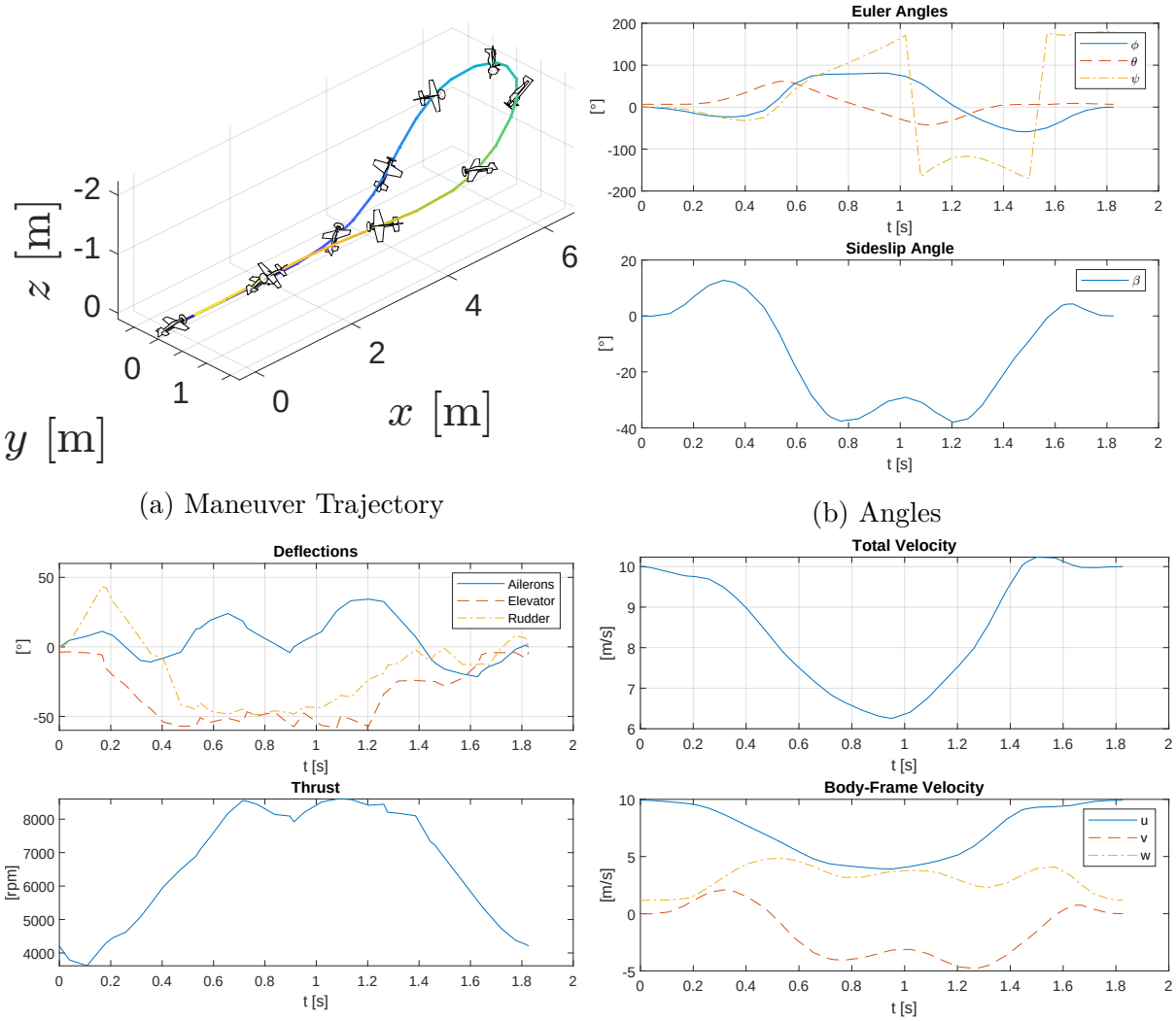

(a) Maneuver Trajectory

(b) Angles

(c) Control Inputs

(d) Velocities

Figure 5.2: Turning Back to the Origin With Euler Angles Constraints

When the pitch and roll angles are constrained, the final time is 28.9% longer than without any constraints. It is illustrated that exceeding 90° in pitch and roll angles helps the aircraft

to turn fast efficiently.

5.1.3 Turn With Height Constraint

In this section, the height is constrained, meaning that the aircraft is not allowed to increase or decrease in height. The final time can be minimized to 1.9061 seconds. The maneuver trajectory, Euler angles, control inputs, and velocities are shown in Fig. 5.3a, 5.3b, 5.3c, and 5.3d, respectively.

It can be observed that the aircraft rolls dramatically to 180°, which makes the lift point downward to control the height. Once again, the sideslip is very large.

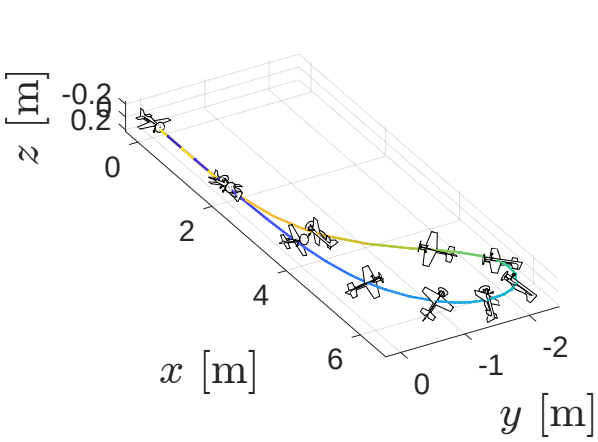

(a) Maneuver Trajectory

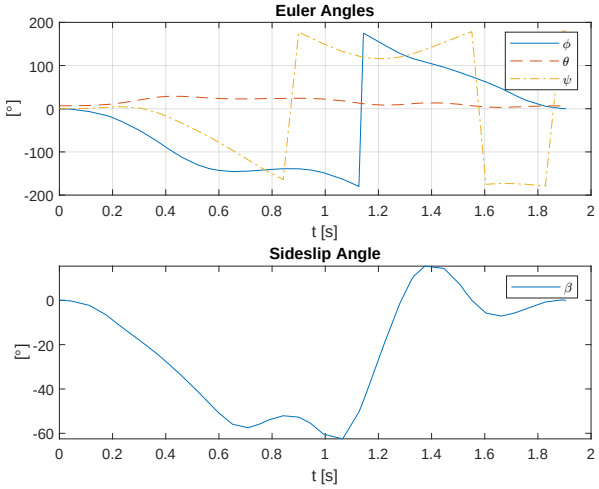

(b) Angles

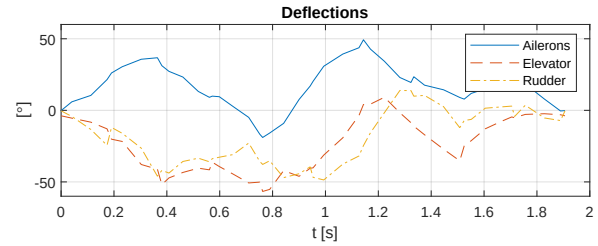

(c) Control Inputs

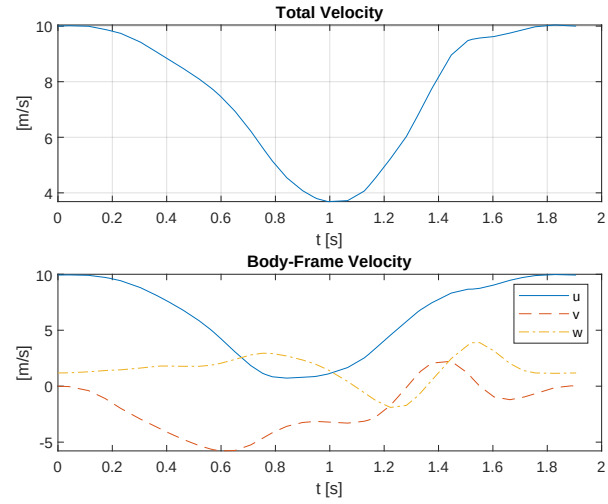

(d) Velocities

Figure 5.3: Turning Back to the Origin With Height Constraints

The coordinated turn was also tested but not shown here due to the limited space. The final time that a coordinated turn can achieve is 2.6336 seconds, which is 85.9% slower than the best case. The coordinated turn does not perform well if the aircraft needs to go back to the origin because of the lack of sideslip angle. The aircraft needs to turn twice to turn around to the exact starting point.

5.2 Turning Without Return to the Origin

In this section, the final position is not specified. The aircraft only needs to turn around. This scenario is meaningful because sometimes the aircraft only needs to turn to the opposite direction but not necessarily back to the starting point.

5.2.1 Turn Without Constraints

In this section, no limits are set. The final time can be minimized to 1.1226 seconds. The maneuver trajectory, Euler angles, control inputs, and velocities are shown in Fig. 5.4a, 5.4b, 5.4c, and 5.4d, respectively.

Unlike in Section 5.1.1, the aircraft does not need to roll to 180 ° to decrease height. However, the aircraft still tends to roll more than 90°, which illustrates that the aircraft is upside down slightly. The hypothesis for this phenomenon is that the optimization tends to generate most force opposite to the original velocity to make the aircraft turn back faster. The aircraft has the tendency to increase the height with certain velocity w shown in Fig. 5.4d. By rolling slightly more than 90°, the aircraft uses the downward component of the lift to resist that tendency. In this maneuver, the sideslip angle is much more moderate than the cases where the aircraft had to return to the starting point, but it is still significant.

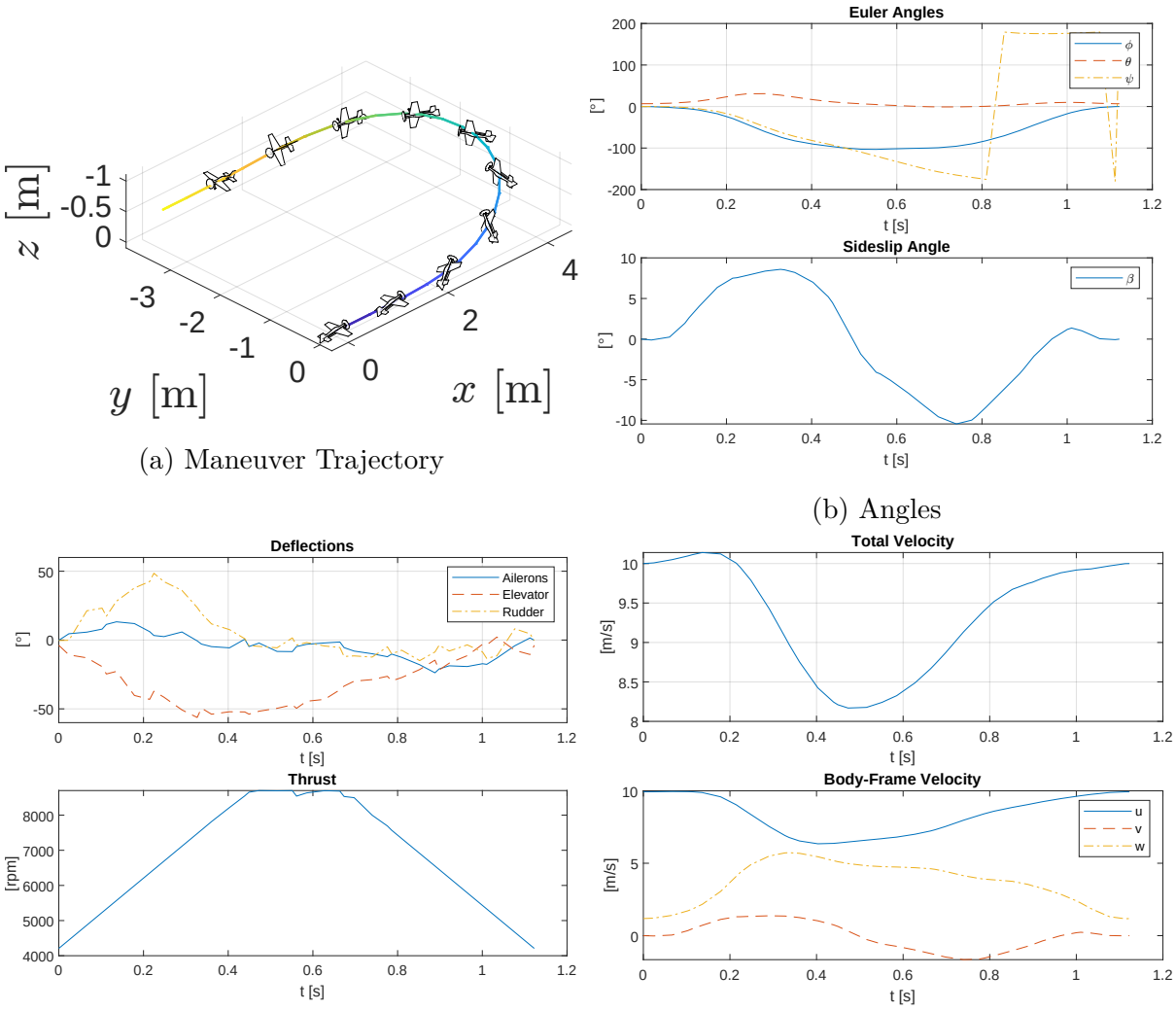

(a) Maneuver Trajectory

(b) Angles

(c) Control Inputs

(d) Velocities

Figure 5.4: Turning Without Return to the Origin Without Constraints

5.2.2 Turn With Height Constraint

In this section, the aircraft is limited to the level height. The final time can be minimized to 1.2888 seconds, which is 14.8% longer than the best case. The maneuver trajectory, Euler angles, control inputs, and velocities are shown in Fig. 5.5a, 5.5b, 5.5c, and 5.5d, respectively. Similar to before, the roll angle exceeds 90° to point the lift slightly downward to control the height. In this case, the sideslip angle becomes quite large.

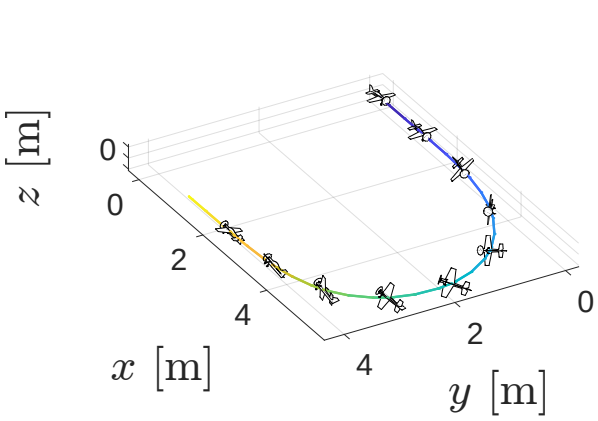

(a) Maneuver Trajectory

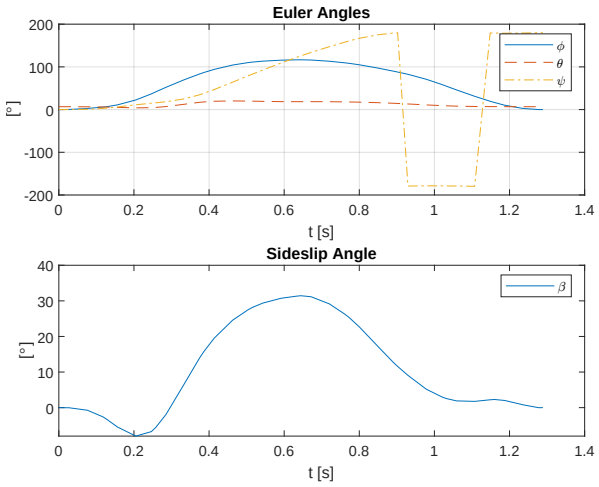

(b) Angles

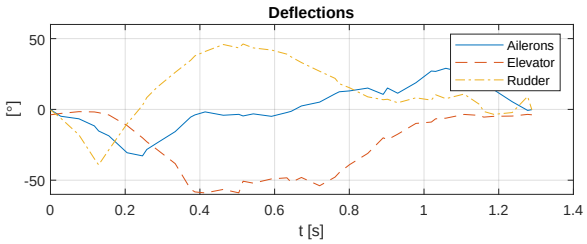

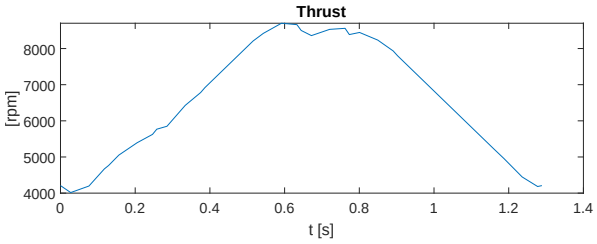

(c) Control Inputs

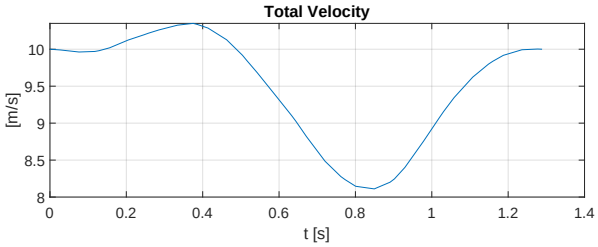

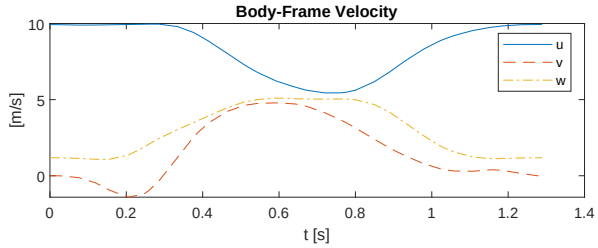

(d) Velocities

Figure 5.5: Turning Without Return to the Origin With Height Constraints

5.2.3 Coordinated Turn

The coordinated turn is conducted in this section by limiting the lateral velocity to be zero. The final time can be minimized to 1.1737 seconds. The maneuver trajectory, Euler angles, control inputs, and velocities are shown in Fig. 5.6a, 5.6b, 5.6c, and 5.6d, respectively.

The sideslip angle shown in Fig. 5.6d also confirms that the aircraft is turning in a coordinated manner. Compared to the two cases shown previously, the total velocity of the coordinated turn drops the least, which implies that the coordinated turn performs more smoothly.

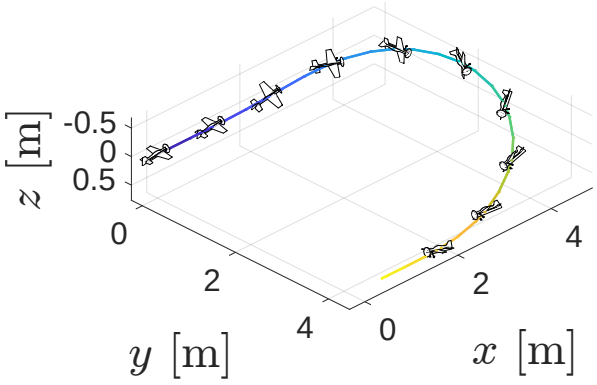

(a) Maneuver Trajectory

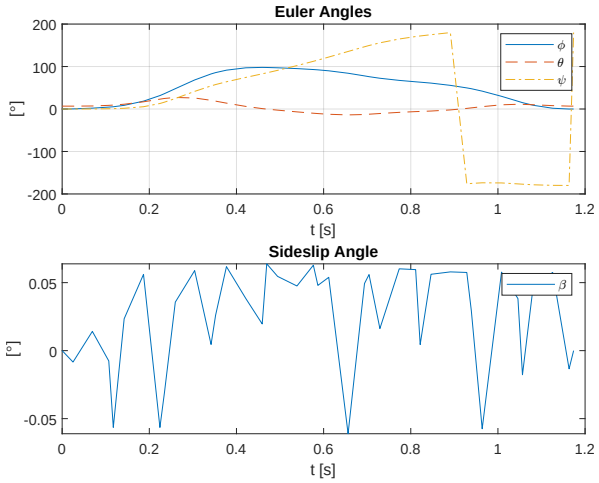

(b) Angles

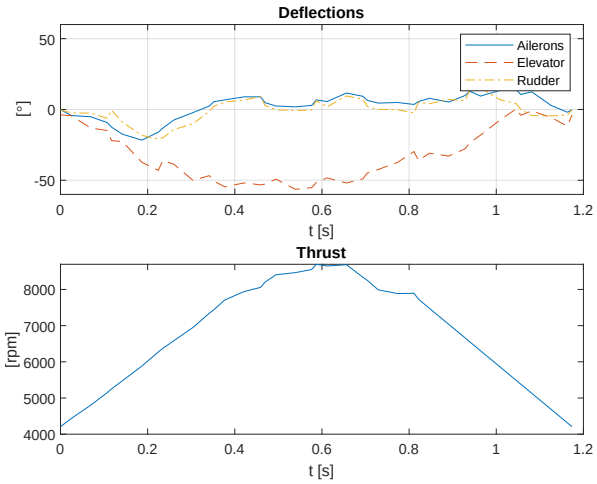

(c) Control Inputs

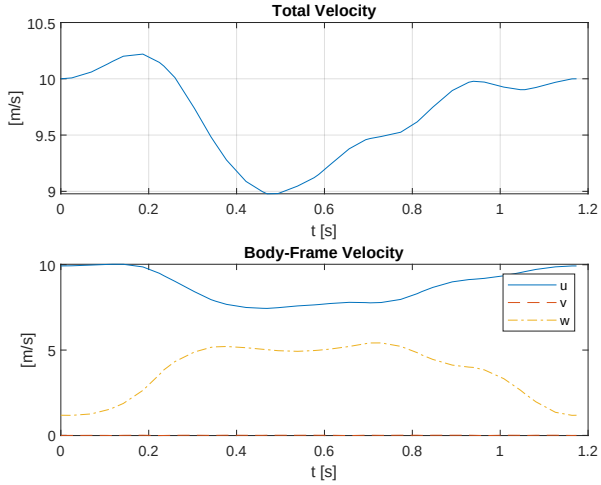

(d) Velocities

Figure 5.6: Turning Without Return to the Origin in Coordinated Turn

Although the coordinated turn does not perform as well as the best case, the difference between them is only 4.6%. The coordinated turn is still considered to be a good turning methodology if the aircraft does not need to return to the origin. Similar to Section 5.1.2, turning with Euler angles constraints are also conducted. The final time is 1.1431 seconds, which is 1.8% slower than the best case. It is not shown here due to limited space.

5.2.4 Flip Back

One possible scenario for this maneuver is that the aircraft approaches the dead end and needs to turn around but there is limited space in the lateral direction. The aircraft cannot perform the usual turning methodology but flips back in a vertical plane. The y in the state vector is constrained within positive or negative 0.01 m for all time. The final time can be minimized to 1.7533 seconds. The maneuver trajectory, Euler angles, control inputs, and velocities are shown in Fig. 5.7a, 5.7b, 5.7c, and 5.7d, respectively. The aircraft pitches up and flips back. It can be noticed that the aircraft rolls and has lateral velocity during the flip back because the final state of the aircraft is still flying straight at velocity of 10 m/s.

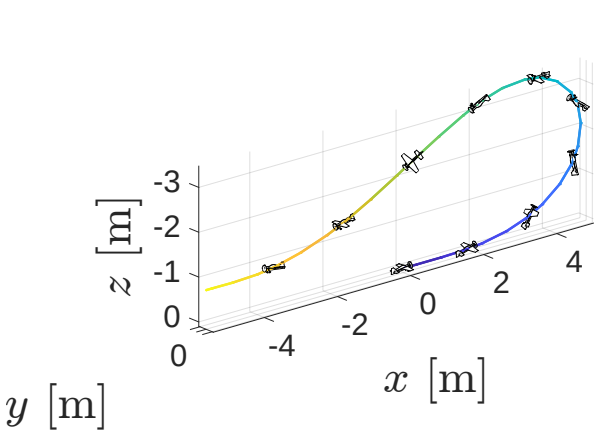

(a) Maneuver Trajectory

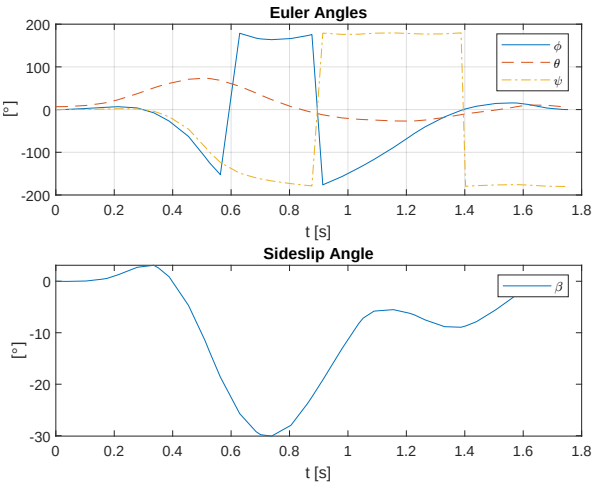

(b) Angles

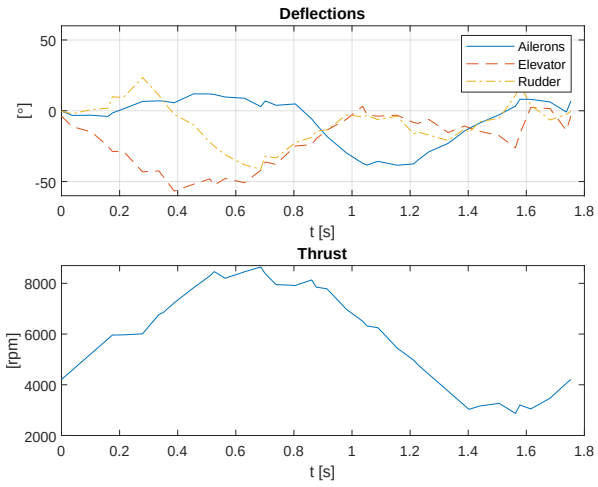

(c) Control Inputs

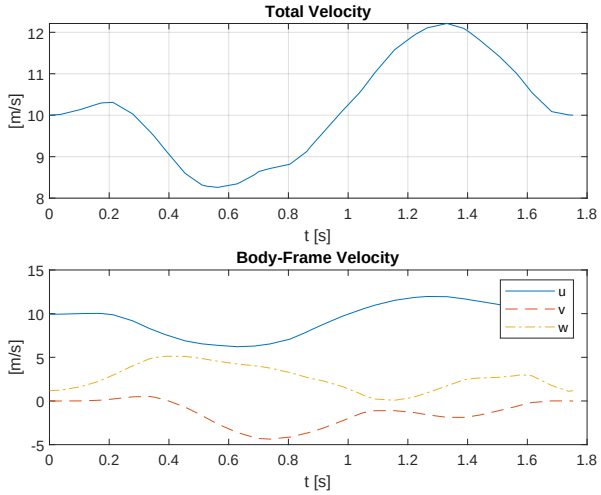

(d) Velocities

Figure 5.7: Flip Back

If the constraint for y is only applied to the final state, the aircraft still tends to perform the normal turning. This is reasonable since the flip back takes more time than the turn around back to the origin. The optimization tends to turn normally if space is not constrained.

Chapter 6

Conclusion

In conclusion, this thesis achieved its original goals of analyzing the UAV turning methodology. The coordinated turn and zero roll turn were assessed and compared in Chapter 3. The trim maneuver of turning was analyzed in Chapter 4. Chapter 5 investigated the agile maneuver of turning around.

Our investigation of turning methodologies led to some interesting results. In the simulation, the coordinated turn performed better in a tighter turn with a smaller radius and higher velocity. Conversely, the zero roll turn performed better in turns with a larger radius and lower velocity. However, since the simulation was performed manually to compare two turning methods, this leaves room for future research because there are other turning methods that can be tested.

After the optimization of the trim maneuver, it was concluded that the coordinated turn performs well in all cases. Some case results showed the existence of some sideslip, but the sideslip angle was typically less than one degree. Additionally, the roll angles seen in the results were close to the angles calculated by the coordinated turn equation, so this verified that the results were close to the coordinated turn.

After the optimization of the agile maneuver, it was determined that the sideslip improved

the turning performance, especially in the turns that need to return to the origin. For this type of turning maneuver, it was remarkable that the unrestricted turn performed 85.9% better than the coordinated turn. However, regarding the instances of turns not going back to the origin, the unrestricted turn was only 4.6% faster than the coordinated turn. Other constraints were also tested. The height constraint proved to limit the performance most significantly. It was hard for the aircraft to turn with limited height.

In summary, the coordinated turn is still considered to be a good turning methodology, except in some special scenarios.

6.1 Recommendations for Future Work

It is suggested to explore the agile maneuver in more depth. In this thesis, the cost functions of agile maneuvers are always set to be the final time because only turning performance is assessed. It is possible to add more terms into the cost function to evaluate the possible changes of the results. For example, the thrust or control surface deflections are possible choices of the cost function. Furthermore, testing different scenarios, such as a 90-degree turn, may lead to valuable results.

Bibliography

[1] A. T. Azar, F. E. Serrano, A. Koubaa, N. A. Mohamed, N. A. Kamal, I. K. Ibraheem, and A. J. Humaidi, "Chapter 19 - sliding mode controller design for unmanned aerial vehicles with unmodeled polytopic dynamics," in *Unmanned Aerial Systems*, ser. Advances in Nonlinear Dynamics and Chaos (ANDC), A. Koubaa and A. T. Azar, Eds. Academic Press, 2021, pp. 495–519. [Online]. Available: https://www.sciencedirect.com/science/article/pii/B9780128202760000261

[2] Y. Ke, K. Wang, and B. M. Chen, "Design and implementation of a hybrid UAV with model-based flight capabilities," *IEEE/ASME Transactions on Mechatronics*, vol. 23, no. 3, pp. 1114–1125, 2018.

[3] K. L. Ross, "Coordinated flight," https://www.friesian.com/flight.htm, 2008.

[4] W. Khan, "Dynamics modeling of agile fixed-wing unmanned aerial vehicles," Ph.D. dissertation, McGill University, Montreal, Canada, 2016.

[5] C. Zheng, L. Li, F. Xu, F. Sun, and M. Ding, "Evolutionary route planner for unmanned air vehicles," *IEEE Transactions on Robotics*, vol. 21, no. 4, pp. 609–620, Aug. 2005. [Online]. Available: https://doi.org/10.1109/tro.2005.844684

[6] F. Fisch, J. Lenz, F. Holzapfel, and G. Sachs, "Trajectory optimization applied to air races," in *AIAA Atmospheric Flight Mechanics Conference*.

American Institute of Aeronautics and Astronautics, Jun. 2009. [Online]. Available: https://doi.org/10.2514/6.2009-5930

[7] T. Matsumoto, A. Konno, R. Suzuki, A. Oosedo, K. Go, and M. Uchiyama, "Agile turnaround using post-stall maneuvers for tail-sitter VTOL UAVs," in *2010 IEEE/RSJ International Conference on Intelligent Robots and Systems*. IEEE, Oct. 2010. [Online]. Available: https://doi.org/10.1109/iros.2010.5650204

[8] A. Noonan, D. Schinstock, C. Lewis, and B. L. Spletzer, "Optimal turning path generation for unmanned aerial vehicles." Sandia National Lab.(SNL-NM), Albuquerque, NM (United States), Tech. Rep., 2007.

[9] J. M. Levin, "Maneuver design and motion planning for agile fixed-wing UAVs," Ph.D. dissertation, McGill University, Montreal, Canada, 2019.

[10] J. B. Russell, *Performance and Stability of Aircraft*. Butterworth Heinemann, 11 1996.

[11] D. E. Kirk, *Optimal control theory: an introduction*. Courier Corporation, 2004.

[12] M. A. Patterson and A. V. Rao, "GPOPS-II: A MATLAB software for solving multiple-phase optimal control problems using hp-adaptive gaussian quadrature collocation methods and sparse nonlinear programming," *ACM Transactions on Mathematical Software*, vol. 41, no. 1, pp. 1–37, Oct. 2014. [Online]. Available: https://doi.org/10.1145/2558904

[13] P. E. Gill, W. Murray, and M. A. Saunders, "SNOPT: An SQP algorithm for large-scale constrained optimization," *SIAM Review*, vol. 47, no. 1, pp. 99–131, Jan. 2005. [Online]. Available: https://doi.org/10.1137/s0036144504446096

[14] J. C. Hernández Ramírez, "Autonomous and semi-autonomous control of agile fixed-wing unmanned aerial vehicles," Ph.D. dissertation, McGill University, Montreal, Canada, 2022.

[15] E. Bulka, "Control and obstacle avoidance for agile fixed-wing aircraft," Ph.D. dissertation, McGill University, Montreal, Canada, 2020.

[16] M. A. Patterson and A. V. Rao, *GPOPS-II: A MATLAB Software for Solving Multiple-Phase Optimal Control Problems*, Dec. 2016. [Online]. Available: https://gpops2.com/resources/gpops2UsersGuide.pdf

Appendix A

Supplementary Information

A.1 Properties of the McFoamy aircraft

Parameter	Symbol	Value	Unit
Mass	m	0.45	kg
Moment of inertia	I_{xx}	0.003922	kg m^2
Moment of inertia	I_{yy}	0.015940	kg m^2
Moment of inertia	I_{zz}	0.019340	kg m^2
Product of inertia	I_{xz}	0.000441	kg m^2
Product of inertia	I_{xy}	0	kg m^2
Product of inertia	I_{yz}	0	kg m^2
Maximum deflection of ailerons	δ_{amax}	52	deg
Maximum deflection of elevator	δ_{emax}	59	deg
Maximum deflection of rudder	δ_{rmax}	49	deg
Minimum rotational speed of propeller	T_{min}	1716	rpm
Maximum rotational speed of propeller	T_{max}	8700	rpm
Maximum aileron deflection rate	$\dot{\delta}_{a_{max}}$	258	deg/s

Maximum elevator deflection rate	$\dot{\delta}_{e_{max}}$	430	deg/s
Maximum rudder deflection rate	$\dot{\delta}_{r_{max}}$	430	deg/s
Maximum rotational acceleration of propeller	$\dot{T}_{max}$	10000	rpm/s

Table A.1: McFoamy parameters

A.2 Detailed equations of motion using quaternions

$$
\begin{aligned}
\dot{u} &= \frac{F_x}{m} + 2g\left(q_2q_4 - q_1q_3\right) + rv - qw \\
\dot{v} &= \frac{F_y}{m} + 2g\left(q_3q_4 + q_1q_2\right) + pw - ru \\
\dot{w} &= \frac{F_z}{m} + g\left(q_1^2 - q_2^2 - q_3^2 + q_4^2\right) + qu - pv \\
\dot{p} &= \frac{I_{zz}M_z + I_{xz}M_z - I_{xz}\left(I_{yy} - I_{xx} - I_{zz}\right)pq - \left(I_{zz}^2 + I_{zz}\left(I_{zz} - I_{yy}\right)\right)qr}{I_{xx}I_{zz} - I_{xz}^2} \\
\dot{q} &= \frac{M_y - \left(I_{xx} - I_{zz}\right)pr - I_{xz}\left(p^2 - r^2\right)}{I_{yy}} \\
\dot{r} &= \frac{I_{zz}M_z + I_{xx}M_z - I_{xz}\left(I_{yy} - I_{zz} - I_{zz}\right)qr - \left(I_{xz}^2 + I_{xx}\left(I_{xx} - I_{yy}\right)\right)pq}{I_{xx}I_{zz} - I_{xz}^2} \\
\dot{q}_1 &= -\frac{1}{2}\left(q_2p + q_3q + q_4r\right) \\
\dot{q}_2 &= \frac{1}{2}\left(q_1p + q_3r - q_4q\right) \\
\dot{q}_3 &= \frac{1}{2}\left(q_1q + q_4p - q_2r\right) \\
\dot{q}_4 &= \frac{1}{2}\left(q_1r + q_2q - q_3p\right) \\
\dot{x} &= u\left(q_1^2 + q_2^2 - q_3^2 - q_4^2\right) + 2v\left(q_2q_3 - q_1q_4\right) + 2w\left(q_1q_3 + q_2q_4\right) \\
\dot{y} &= 2u\left(q_2q_3 + q_1q_4\right) + v\left(q_1^2 - q_2^2 + q_3^2 - q_4^2\right) + 2w\left(q_3q_4 - q_1q_2\right) \\
\dot{z} &= 2u\left(q_2q_4 - q_1q_3\right) + 2v\left(q_3q_4 + q_1q_2\right) + w\left(q_1^2 - q_2^2 - q_3^2 + q_4^2\right)
\end{aligned}
\tag{A.1}
$$

A.3 Detailed Plot

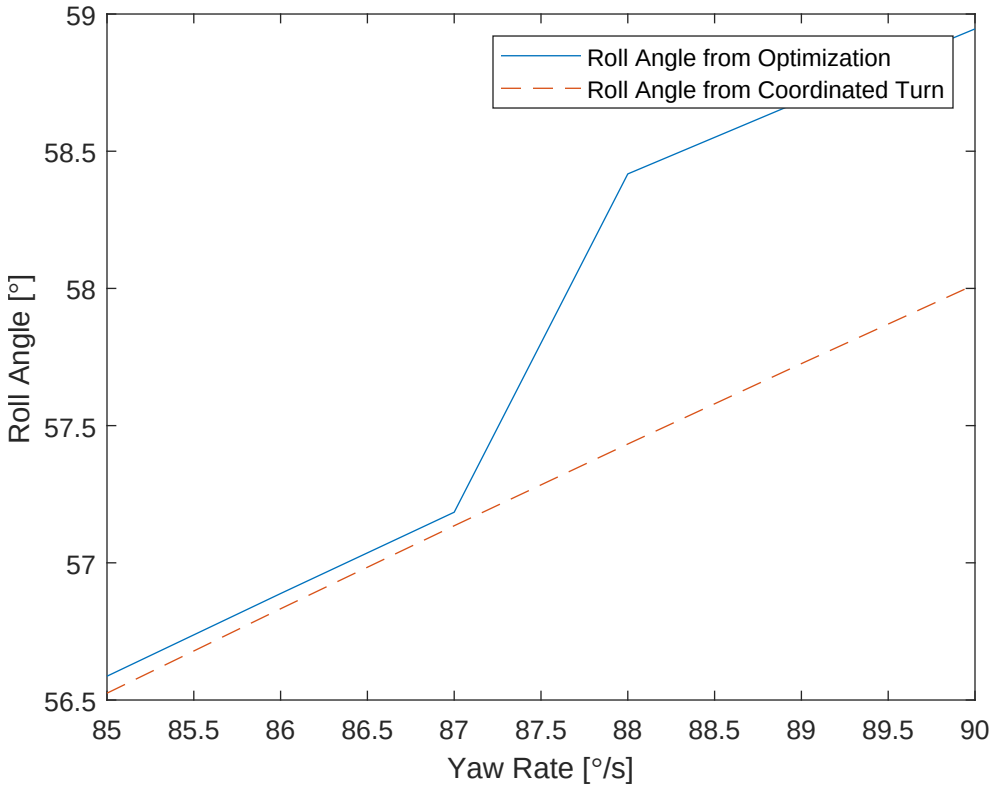

Figure A.1: Detailed plot of the roll angle vs. yaw rate

A.4 Setup for the straight level flight

The desired velocity is $V_d = 10m/s$. The cost function is:

$$J = \int_{t_0}^{t_f} (V - V_d)^2 + \dot{q}^2 + \dot{\theta}^2 + {\delta_a}^2 + {\delta_a}^2 \mathrm{d}tV \quad = u^2 + v^2 + w^2 \tag{A.2}$$

The dynamics constraints are not changed as in Chapter 4. The path constraint, Eq. 2.10, becomes:

$$\mathbf{u} = [\dot{\delta}_a,\ \dot{\delta}_e,\ \dot{\delta}_r,\ \dot{T}]^T = \mathbf{0} \tag{A.3}$$

The endpoint constrain is:

$$\sqrt{u\left(t_0\right)^2 + v\left(t_0\right)^2 + w\left(t_0\right)^2} = V_d \tag{A.4}$$

The results are used to form the conditions for Chapter 5:

$$\begin{aligned}
\mathbf{x}\left(t_0\right) &= [u_0,\ v_0,\ w_0,\ 0,\ 0,\ 0,\ q_{10},\ q_{20},\ q_{30},\ q_{40},\ 0,\ 0,\ 0,\ \delta_{a0},\ \delta_{e0},\ \delta_{r0},\ T_0]^T \\
\mathbf{x}\left(t_f\right) &= [u_0,\ v_0,\ w_0,\ 0,\ 0,\ 0,\ q_{1f},\ q_{2f},\ q_{3f},\ q_{4f},\ x_f,\ y_f,\ z_f,\ \delta_{a0},\ \delta_{e0},\ \delta_{r0},\ T_0]^T
\end{aligned} \tag{A.5}$$

$$\begin{aligned}
u_0 &= 9.9301 m/s \\
v_0 &= 0\ m/s \\
w_0 &= 1.1805\ m/s \\
q_{10} &= 0.9983 \\
q_{20} &= 0 \\
q_{30} &= 0.0591 \\
q_{40} &= 0 \\
q_{1f} &= 0 \\
q_{2f} &= 0.0591 \\
q_{3f} &= 0 \\
q_{4f} &= -0.9983 \\
\delta_{a0} &= -0.0032\ rad \\
\delta_{e0} &= -0.0667\ rad \\
\delta_{r0} &= -0.0061\ rad \\
T_0 &= 4208\ rpm
\end{aligned} \tag{A.6}$$

A.5 Validation of the code

The simulation model is validated by performing some tasks and compared with the experimental data.

One simple case is shown here. When the velocity of [22.5, 0, 0] inputted into the model with 8700 rpm in the thrust and others remain zero. The model confirms that the forces are almost zero, which indicates the maximum velocity condition. The maximum velocity in the model is around 22 m/s.

$$\begin{aligned} [F_x,\ F_y,\ F_z,\ M_x,\ M_y,\ M_z] &= M\,[\delta_a,\ \delta_e,\ \delta_r,\ T,\ u,\ v,\ w,\ p,\ q,\ r] \\ [0.2179,\ 0,\ 0,\ -0.0212,\ 0.0135,\ 0] &= M\,[0,\ 0,\ 0,\ 8700,\ 22.5,\ 0,\ 0,\ 0,\ 0,\ 0] \end{aligned} \tag{A.7}$$

The maximum velocity from the experiment is around 17 m/s. It can be seen that there exists some difference between the model and the experimental data, which is reasonable due to some disturbances, such as unexpected wind. The validation shown here is simplified due to limited space. The optimization for maximum velocity should provide a more accurate result. The detailed model validation can be found in [15].

The optimization platform, GPOPS [12], combined with the NLP solver, SNOPT [13], is validated by testing the examples shown in the GPOPS manual [16].